BRAIN
ORIGINAL ARTICLE

Visualizing reactive astrocyte-neuron interaction in Alzheimer's disease using ^{11}C-acetate and ^{18}F-FDG

Min-Ho Nam,[1,2,†] Hae Young Ko,[3,†] Dongwoo Kim,[3,†] Sangwon Lee,[3] Yongmin Mason Park,[4,5] Seung Jae Hyeon,[1] Woojin Won,[4] Jee-In Chung,[3] Seon Yoo Kim,[3] Han Hee Jo,[3] Kyeong Taek Oh,[6] Young-Eun Han,[1] Gwan-Ho Lee,[7] Yeon Ha Ju,[1,4,5] Hyowon Lee,[1] Hyunjin Kim,[1,2] Jaejun Heo,[1] Mridula Bhalla,[4,5] Ki Jung Kim,[4] Jea Kwon,[4] Thor D. Stein,[8] Mingyu Kong,[9] Hyunbeom Lee,[9] Seung Eun Lee,[7] Soo-Jin Oh,[1] Joong-Hyun Chun,[3] Mi-Ae Park,[10] Ki Duk Park,[1] Hoon Ryu,[1,8] Mijin Yun[3] and C. Justin Lee[4,5]

[†]These authors equally contributed to this work.

Reactive astrogliosis is a hallmark of Alzheimer's disease (AD). However, a clinically validated neuroimaging probe to visualize the reactive astrogliosis is yet to be discovered. Here, we show that PET imaging with ^{11}C-acetate and ^{18}F-fluorodeoxyglucose (^{18}F-FDG) functionally visualizes the reactive astrocyte-mediated neuronal hypometabolism in the brains with neuroinflammation and AD.

To investigate the alterations of acetate and glucose metabolism in the diseased brains and their impact on the AD pathology, we adopted multifaceted approaches including microPET imaging, autoradiography, immunohistochemistry, metabolomics, and electrophysiology. Two AD rodent models, APP/PS1 and 5xFAD transgenic mice, one adenovirus-induced rat model of reactive astrogliosis, and post-mortem human brain tissues were used in this study. We further curated a proof-of-concept human study that included ^{11}C-acetate and ^{18}F-FDG PET imaging analyses along with neuropsychological assessments from 11 AD patients and 10 healthy control subjects.

We demonstrate that reactive astrocytes excessively absorb acetate through elevated monocarboxylate transporter-1 (MCT1) in rodent models of both reactive astrogliosis and AD. The elevated acetate uptake is associated with reactive astrogliosis and boosts the aberrant astrocytic GABA synthesis when amyloid-β is present. The excessive astrocytic GABA subsequently suppresses neuronal activity, which could lead to glucose uptake through decreased glucose transporter-3 in the diseased brains. We further demonstrate that ^{11}C-acetate uptake was significantly increased in the entorhinal cortex, hippocampus and temporo-parietal neocortex of the AD patients compared to the healthy controls, while ^{18}F-FDG uptake was significantly reduced in the same regions. Additionally, we discover a strong correlation between the patients' cognitive function and the PET signals of both ^{11}C-acetate and ^{18}F-FDG.

We demonstrate the potential value of PET imaging with ^{11}C-acetate and ^{18}F-FDG by visualizing reactive astrogliosis and the associated neuronal glucose hypometablosim for AD patients. Our findings further suggest that the acetate-boosted reactive astrocyte-neuron interaction could contribute to the cognitive decline in AD.

1 Brain Science Institute, Korea Institute of Science and Technology (KIST), Seoul 02792, Republic of Korea
2 Department of KHU-KIST Convergence Science and Technology, Kyung Hee University, Seoul 02447, Republic of Korea
3 Department of Nuclear Medicine, Severance Hospital, Yonsei University College of Medicine, Seoul 03722, Republic of Korea

Received August 25, 2022. Revised January 04, 2023. Accepted January 23, 2023. Advance access publication April 17, 2023

4 Center for Cognition and Sociality, Institute for Basic Science, Daejeon 34126, Republic of Korea
5 IBS School, University of Science and Technology, Daejeon 34126, Republic of Korea
6 Department of Medical Engineering, Yonsei University College of Medicine, Seoul 03722, Republic of Korea
7 Research Resources Division, KIST, Seoul 02792, Republic of Korea
8 Boston University Alzheimer's Disease Research Center and Department of Pathology, Chobanian and Avedisian Boston University School of Medicine, Boston, MA 02130, USA
9 Molecular Recognition Research Center, KIST, Seoul 02792, Republic of Korea
10 Department of Radiology, UT Southwestern Medical Center, Dallas, TX 75390, USA

Correspondence to: C. Justin Lee, PhD
IBS Center for Cognition and Sociality
55 Expo-ro, Doryong-dong, Yuseong-gu
Daejeon 34126, Republic of Korea
E-mail: cjl@ibs.re.kr

Correspondence may also be addressed to: Mijin Yun, MD, PhD
Severance Hospital, Yonsei University College of Medicine
50-1, Yonsei-Ro, Seodaemun-gu, Seoul 03722
Republic of Korea
E-mail: yunmijin@yuhs.ac

Hoon Ryu, PhD
KIST Brain Science Institute
5 Hwarangro-14-gil, Seongbuk-gu
Seoul 02792, Republic of Korea
E-mail: hoonryu@kist.re.kr

Keywords: Alzheimer's disease; ^{11}C-Acetate; ^{18}F-Fluorodeoxyglucose; monocarboxylate transporter 1 (MCT1); PET imaging; reactive astrocyte

Introduction

Astrocytes support neighbouring neurons both physically and chemically in physiological conditions. However, in response to various physical and chemical insults, astrocytes dynamically change their properties morphologically, molecularly and functionally.[1] The responding astrocytes are termed reactive astrocytes. Reactive astrogliosis, a hallmark of neuroinflammation in Alzheimer's disease (AD), often precedes neuronal degeneration or death.[2,3] Several previous studies even demonstrated that reactive astrogliosis can directly cause extensive neuronal death.[4–6] Recent studies further reported that reactive astrocytes aberrantly produce GABA to inhibit neighbouring neuronal activity and glucose metabolism,[7–10] which critically contributes to neuronal dysfunction in AD.[7,11] Therefore, *in vivo* imaging of reactive astrogliosis should have a considerable diagnostic value at the early stages of AD. Based on recent reports demonstrating the abundant expression of monoamine oxidase B (MAO-B) in the reactive astrocytes of AD,[7,10] PET of MAO-B has received some endorsement for the *in vivo* imaging of reactive astrogliosis.[12] However, several reports have expressed concerns that MAO-B may not be entirely specific for reactive astrogliosis due to its basal expression in certain types of neurons in the human brain.[13–15] These concerns necessitate the identification of an advanced molecular target for PET imaging of reactive astrogliosis.

Acetate has been known as an astrocyte-specific energy substrate and an attractive alternative to glucose.[16–19] Acetate has long been believed to be tightly associated with astrocytic metabolism or astrocytic activity,[19] despite a conflicting report.[20] A few previous studies have demonstrated an escalated acetate metabolism in several neuroinflammatory disorders.[21,22] However, whether and how acetate metabolism is associated with astrocyte reactivity has not yet been elucidated. Moreover, acetate is not clinically applied as a PET tracer for AD. In the current study, we investigated the causal relationship between astrocytic acetate metabolism, astrocyte reactivity, and neuronal glucose metabolism in the adenovirus-induced reactive astrogliosis model and two different transgenic AD mouse models. We further investigated whether and how astrocytic acetate metabolism contributes to the impaired hippocampal function and memory deficits in AD mouse models. Finally, we investigated the feasibility of imaging reactive astrogliosis, which leads to neuronal hypometabolism in the brains of AD patients, by employing radioactive acetate and glucose as molecular probes.

Materials and methods

Animals

Adult male Sprague Dawley rats (Koatech) weighing 250–300 g (8 to 10 weeks old) were used for experiments with adenovirus-induced reactive astrogliosis models. For *in vivo* investigation, we used adenovirus-induced neuroinflammation rat models (8 to 10 weeks old) as previously demonstrated,[8] adult male APP/PS1 (6 to 25 months old), and 5xFAD transgenic mice (6 to 11 months old). Animal care was followed by National Institutes of Health (NIH) guidelines. The animal experimental procedures were approved by Institutional Animal Care and Use Committee of Korea Institute of Science and Technology (KIST; Seoul, Korea; approval No. KIST-2019-042), and Yonsei University (Seoul, Korea; approval No. 2017-0187). The animals were kept on a 12-h light-dark cycle

with controlled temperature (21 ± 1°C) and humidity (50 ± 10%) and had *ad libitum* access to food and water. KDS2010, a MAO-B inhibitor, was synthesized as previously described.[10] KDS2010 was administered by dissolving the compound in drinking water for 9 days after baseline micro-PET imaging. The amount of KDS2010 was calculated as 10 mg/kg daily.

Primary astrocyte culture

The cerebral cortex of a P1 pup was dissected free of adherent meninges, minced and dissociated into single-cell suspension by trituration through a Pasteur pipette. Dissociated cells were plated onto either 12-mm glass coverslips or six-well plates coated with 0.1 mg/ml poly-D-lysine (PDL; Sigma). Cells were grown in Dulbecco's modified Eagle medium (DMEM; Gibco) supplemented with 25 mM glucose, 10% heat-inactivated horse serum, 10% heat-inactivated foetal bovine serum, 2 mM glutamine, and 1000 units/ml penicillin-streptomycin. Three days later, cells were vigorously washed with repeated pipetting using medium and the media was replaced to get rid of debris and other floating cell types.

Lipopolisaccharide (LPS, 20 ng/ml) and interferon-gamma (IFN-γ, 10 ng/ml) were treated onto primary cultured astrocytes for 24 h for quantitative reat-time PCR (qRT-PCR).

For amyloid-β oligomerization, human amyloid-β 1–42 peptides (Aβ, ab120301, Abcam) were dissolved into DMSO (10 mM) and further diluted to 1 mM with DPBS. Diluted Aβ was incubated at 37°C for 1 week and stored at −80°C till further use. The prepared amyloid-β (1 μM) was treated onto primary cultured astrocytes for 5 days for sniffer patch, qRT-PCR and RNA sequencing.

MCT1-shRNA development

For gene-silencing of *Slc16a1* (coding MCT1 protein), we prepared MCT1-shRNA whose sequences of complementary oligomers were 5′-TGC TCC ACT TAA TCA GGC TTT CTT CAA GAG AGA AAG CCT GAT TAA GTG GAG CTT TTT TC-3′ and 3′-TCG AGA AAA AAG CTC CAC TTA ATC AGG CTT TCT CTC TTG AAG AAA GCC TGA TTA AGT GGA GCA-5′. The knockdown efficiency was tested by reverse transcription polymerase chain reaction (RT-PCR) with cDNA from rat primary cultured astrocytes, which were electroporated with the shRNA vector. For AAV-based shRNA expression, a lentiviral vector containing the MCT1-shRNA gene was constructed into the HpaI–XhoI restriction enzyme sites of the pSico AAV vector in an AAV-DJ capsid.

Virus preparation and injection

To induce reactive astrogliosis, we used the Adeno-GFAP-GFP virus, which contains the *GFP* gene under control of the *GFAP* promoter sequence, as described previously.[8] We injected Adeno-GFAP-GFP into two points in the sensory cortex (AP = −2.0 mm, ML = +2.0 mm and +4.0 mm, DV = −1.5 mm and −2.5 mm from bregma) using stereotaxic apparatus under general anaesthesia with 2% isoflurane. AAV-DJ was engineered via DNA family shuffling technology, which created a hybrid capsid from eight AAV serotypes. AAV-DJ displays a higher transduction efficiency *in vitro* than any wild-type serotype. AAV-DJ is known to successfully infect a broad range of various cell types *in vivo*.[23] The viral vectors were purified by iodixanol gradients by the KIST Virus Facility. The minimum number of viral particles was 1.0×10^{12} genome copies (GC)/ml, which is a concentrated virus package. The detailed titre information is listed in Supplementary Table 4. To selectively knockdown astrocytic MCT1, we injected AAV-GFAP-Cre-mCherry and AAV_{DJ} containing pSico-MCT1-shRNA-GFP (or pSico-scrambled-shRNA-GFP for control) into the same points in the sensory cortex using stereotaxic apparatus. A mixture of 1 μl of adenovirus for inducing reactive astrogliosis, 0.5 μl of AAV-GFAP-Cre-mCherry, and 0.5 μl of pSico-MCT1-shRNA-GFP for knockdown astrocytic MCT1, was slowly injected at the target sites with a rate of 0.15 ml/min using 33G Hamilton syringe connected to an UltraMicroPump (WPI). After injection, the needle was left in place for an additional 7 min before being slowly retracted.

In vitro ^{14}C-acetate and ^{14}C-deoxyglucose uptake assays in primary astrocytes

To measure ^{14}C-acetate uptake, primary astrocytes were seeded in 24-well plates and incubated with a standard culture medium for 24 h. For the inhibition test of SR13800 (Tocris), the cells were incubated in 0, 10, 100 and 1000 nM of SR13800 with culture medium at 37°C for 12 h. Subsequently ^{14}C-acetate (59.0 mCi/mmol, PerkinElmer) 1 μCi/ml of external solution (150 mM NaCl, 3 mM KCl, 10 mM HEPES, 22 mM sucrose, 2 mM $MgCl_2$, 2 mM $CaCl_2$, pH 7.4) were added to each wells and the cells were incubated at 37°C for 20 min. To measure ^{14}C-deoxyglucose (^{14}C-DG) uptake, primary neurons were seeded in 24-well plates and incubated with neuron culture medium. At 14 days after plating, ^{14}C-DG (53.5 mCi/mmol, PerkinElmer) 1 μCi/ml of glucose-free DMEM containing 0.5 mM glucose were added to each wells and the cells were incubated at 37°C for 20 min. At the end of the uptake period, each well was washed twice with ice-cold PBS. The cells were lysed with 200 μl of 0.2 N NaOH for 2 h at room temperature. After the addition of a scintillation cocktail (Ultima Gold, PerkinElmer), the radioactivity was measured by a liquid scintillation counter (Tri-Carb, PerkinElmer). The measured radioactivity was normalized to protein concentration which was performed using a BCA Protein Assay kit (Thermo Fisher Scientific). Experiments were performed three times using three replicates for each experimental condition.

Immunostaining for confocal microscopy

For immunohistochemistry, sections were first incubated for 1.5 h in a blocking solution (0.3% Triton-X, 2% goat serum, and 2% donkey serum in 0.1 M PBS) and then immunostained with a mixture of primary antibodies in a blocking solution at 4°C. Primary antibodies used are as follows: chicken anti-GFAP (1:500, ab5541, Millipore), rabbit anti-MCT1 (1:200, ab3538p, Millipore) for rat samples, rabbit anti-MCT1 (1:200, AMT-011, Alomone) for mouse samples, mouse anti-NeuN (1:1000, MAB377, Millipore), mouse anti-GLUT3 (1:200, sc-74399, Santa Cruz) for rat samples, rabbit anti-GLUT3 (1:200, AGT-023, Alomone) for mouse samples, and guinea pig anti-GABA (1:300, ab175, Millipore). After extensive washing, sections were incubated with corresponding fluorescent secondary antibodies for 2 h and then washed with PBS three times. If needed, DAPI (1:3000, Pierce) staining was performed. To visualize amyloid plaques, sections were incubated in 1 mM thioflavin-S, which had been dissolved in 50% ethanol for 8 min. Sections were rinsed with 80% ethanol twice for differentiation and washed with PBS three times. Finally, sections were mounted with a fluorescent mounting medium (S3023, Dako) and dried. A series of fluorescent images were obtained with an A1 Nikon confocal microscope, and z-stack images in 3-μm steps were processed for further analysis using or NIS-Elements (Nikon) software and ImageJ program (NIH). Any alterations in brightness or contrast were equally applied to the entire image set. Specificity of primary antibody and

immunoreaction was confirmed by omitting primary antibodies or changing fluorescent probes of the secondary antibodies.

For immunocytochemistry, we fixed the cultured astrocytes with 4% paraformaldehyde (PFA) at 4°C for 10 min. After washing with 0.1 M PBS three times, we performed immunocytochemistry according to the same procedures as immunohistochemistry.

Western blotting

The cells were lysed with 1% sodium dodecyl sulphate (SDS) lysis buffer containing protease inhibitor cocktail (Roche), and total protein concentration was determined by protein assay (Thermo Fisher Scientific). Equal amounts (5 μg) of protein from each sample were separated by SDS-polyacrylamide gel electrophoresis (SDS-PAGE, Bio-Rad) and transferred to polyvinylidene difluoride membranes (Millipore). The membranes were blocked with 5% skim milk at room temperature for 1 h and then incubated with rabbit anti-MAO-B (1:1000, Novus), rabbit anti-MCT1 (1:1000, Alomone), rabbit anti-GFAP (1:3000, Dako), and mouse anti-beta actin (1:2000, Invitrogen) at 4°C overnight. Membranes were washed in TBS-T and incubated with goat anti-rabbit or anti-mouse IgG horseradish peroxidase (1:2000, GeneTex) as the secondary antibody. The antigen-antibody complexes were visualized using the ECL western blotting substrate (Thermo Fisher Scientific).

Quantitative real-time RT-PCR

Total RNAs were isolated from the frozen brain tissues using TRIzol™ reagent (TR118, MRC). Fifty nanograms of RNA was used as a template for quantitative RT-PCR amplification, using SYBR Green Real-time PCR Master Mix (QPK-201, Toyobo). Primers were standardized in the linear range of the cycle before the onset of the plateau. Human GAPDH was used as an endogenous control to standardize the amount of RNA in each reaction. The following sequences of primers were used. *MCT1* forward: 5′-TAC CTC CAG ACT CTC CTG GC -3′; *MCT1* reverse: 5′-GTC CCC TCC GCA AAG TCT AC-3′; *GAPDH* forward: 5′- GAA ATC CCA TCA CCA TCT TCC-3′ and reverse: 5′- GAG GCT GTT GTC ATA CTT CTC-3′.

^{11}C-acetate preparation

Preparation of [1-^{11}C]acetate was accomplished on a commercial automatic radiosynthetic module (GE Tracerlab FXc-pro). [1-^{11}C]CO_2 produced from a PETtrace 860 cyclotron (GE Healthcare), by bombardment (50 μA of 16.5 MeV protons, 10–20 min) of $^{14}N_2$ target gas containing 0.1% O_2 was bubbled into a solution of methylmagnesium chloride Grignard reagent for 3 min, followed by hydrolysis with 1 mM acetic acid. Purification on solid phase extraction cartridges (IC-H, IC-Ag, and SAX cartridges) afforded [1-^{11}C]acetate formulated in 0.9% saline solution (12–18 GBq). All QC release criteria (appearance, radiochemical identity, radiochemical purity, chemical purity, pH, endotoxins, filter integrity and sterility) were determined and passed within the acceptance range. The specific activity of produced [1-^{11}C]acetate was >18.5 GBq/μmol. ^{11}C was radiolabelled at carboxylic carbon of the acetate.

MicroPET imaging

Each rat was scanned a total of four times: baseline ^{11}C-acetate and baseline ^{18}F-FDG scans prior to adenovirus injection, ^{11}C-acetate scan, and ^{18}F-FDG scan at 8 days after adenovirus injection. KDS2010 (10 mg/kg/day) was administered for 9 days after the baseline PET image. To minimize the effect of glycaemia, all animals were fasted overnight before PET imaging. Rat imaging was performed using a microPET scanner (Inveon, Siemens Healthcare), which has a transaxial resolution of 1.4 mm full-width at half-maximum and a 12.7 mm field of view. Animals were anaesthetized with 2.5% isoflurane before the administration of radiotracer. A dose of 37 MBq (1 mCi/200 ml in saline) of ^{11}C-acetate was injected into the tail vein of the rats. Following the 20 min of uptake time, ^{11}C-acetate PET data were acquired for 40 min under 2% isoflurane anaesthesia. This protocol was supported by our preliminary dynamic study of ^{11}C-acetate in the control and adenovirus-injected rats demonstrating ^{11}C-acetate level is well stabilized between 10–20 min after injection (data not shown). For the ^{18}F-FDG PET scan, the rats were administered with 20 MBq (0.54 mCi/200 ml in saline) of ^{18}F-FDG and allowed to uptake for 40 min on a heating pad under 2% isoflurane anaesthesia. Then, 40 min static acquisition was performed for ^{18}F-FDG PET scan. All PET data were reconstructed with 3D ordered subset expectation-maximization (OSEM) with two iterations and 18 subsets. The voxel size was $0.385 \times 0.385 \times 0.796$ mm^3 and the matrix size was $256 \times 256 \times 159$.

MicroPET image processing was performed using the Analysis of Functional NeuroImages (AFNI) software.[24] ^{11}C-acetate and ^{18}F-FDG PET images were registered to the MRI template of Sprague Dawley rat brain using an automated template-based registration algorithm and manual manipulation for minor misalignment.[25] To statistically compare ^{11}C-acetate and ^{18}F-FDG PET images in the adenovirus-induced reactive astrogliosis models (with and without KDS2010 treatment, and with and without scrambled-shRNA and MCT1-shRNA), a voxel-wise *t*-test was performed using 3dttest in AFNI software (statistical threshold, $P < 0.01$). The 3D rendering images fused T_1-weighted magnetic resonance image with the statistical parametric map were displayed using MRIcroGL software (https://www.mccauslandcenter.sc.edu/mricrogl/).

Electrophysiology

Sniffer patch

For sniffer patch, we used GABAc sensor cells, which were prepared as previously described,[7,10] and primary cultured cortical astrocytes. The day before the sniffer patch, cortical astrocytes were seeded from culture dishes onto 12-mm PDL-coated glass coverslips in 24-well plates. On the day of the sniffer patch, sensor cells were seeded from culture dishes onto astrocyte-placed coverslips. Astrocytes, which were co-cultured with GABAc receptor sensor cell, were incubated with 5 mM Fura-2AM (mixed with 5 μl of 20% pluronic acid; P3000MP, Invitrogen) for 40 min and washed at room temperature and subsequently transferred to a microscope stage for imaging. External solution contained (in mM): 150 NaCl, 10 HEPES, 3 KCl, 2 $CaCl_2$, 2 $MgCl_2$, pH adjusted to pH 7.3 and osmolality to 320–325 mOsm/kg. For Ca^{2+} imaging, intensity images of 510 nm wavelength were taken at 340 and 380 nm excitation wavelengths using CoolLED (pE-340^{fura}). Astrocytic Ca^{2+} responses were induced by poking as previously described.[26] Two resulting images were used for ratio calculations in Imaging Workbench version 9.0 (INDEC biosystems). GABAcR-mediated currents from sensor cell were recorded under voltage clamp (Vh = −50 mV) using Multiclamp 700B amplifier (Molecular Devices), acquired with pClamp 11.0.3 (Molecular Devices) Recording electrodes (4–7 MΩ) were filled with (mM): 140 CsCl, 0.5 $CaCl_2$, 10 HEPES, and 10 EGTA (pH adjusted to 7.3 with CsOH and Osmolality with 285–295 mOsm/kg). To normalize the different expressions of GABAc in sensor cells, 100 μM of GABA bath application was performed to obtain

maximal GABAc current from each sensor cells. Sniffed current, which is mediated by released GABA from astrocytes, was divided by maximal GABAc current.

Tonic GABA recording

For *ex vivo* electrophysiology of dentate granule cells, 300-μm thick hippocampal horizontal acute slices were prepared as previously described,[10] and maintained at room temperature in a submerged chamber with extracellular artificial CSF (ACSF) solution [126 mM NaCl, 24 mM $NaHCO_3$, 1 mM NaH_2PO_4, 2.5 mM KCl, 2.5 mM $CaCl_2$, 2 mM $MgCl_2$, and 10 mM d-(+)-glucose (pH 7.4)]. The tonic GABA recording was performed as previously described.[10] Briefly, we performed whole-cell recordings from dentate granule cell somata at holding potential of −70 mV. Pipette resistance was typically 6 to 8 MΩ. The pipette was filled with the internal solution [135 mM CsCl, 4 mM NaCl, 0.5 mM $CaCl_2$, 10 mM HEPES, 5 mM EGTA, 2 mM Mg-adenosine triphosphate, 0.5 mM Na_2-guanosine triphosphate, and 10 mM QX-314, pH adjusted to 7.2 with CsOH (osmolarity, 278 to 285 mOsm)]. For the stabilized baseline current, d-AP5 (50 μM) and CNQX (20 μM) was treated. When the current is stabilized, bicuculline (100 μM) was treated to reveal the tonic GABA current. The amplitude of tonic GABA currents was measured by the baseline shift after bicuculline administration using Clampfit program. Frequency and amplitude of spontaneous inhibitory postsynaptic currents before bicuculline administration were detected and measured by MiniAnalysis (Synaptosoft).

Evoked spike probability

Evoked spike probability recordings were performed in the same settings above and as described previously.[10] Briefly, electrical stimulation was given by tungsten bipolar electrode placed in the outer half of the middle third molecular layer of dentate gyrus. Stimulus intensity was set by 0.1 Hz stimulation of lateral perforant path fibres (100-μs duration; 100 to 1000 μA intensity). The evoked excitatory postsynaptic potentials (EPSPs) were recorded using glass pipette electrodes filled with internal solution [120 mM potassium gluconate, 10 mM KCl, 1 mM $MgCl_2$, 0.5 mM EGTA, 40 mM HEPES (pH 7.2)]. Spiking probability was calculated as the ratio of the number of successful (spike-generating) stimulations to the total number of stimulations.

Liquid-chromatography mass-spectroscopy

Drug-treated cortical astrocytes [days *in vitro* (DIV) 12–13] were detached from culture dishes by incubating 2.5% trypsin (15140-122, Gibco). Trypsinized astrocytes were washed with Dulbecco's phosphate-buffered saline (DPBS, LB001-02, Welgene). Washed astrocyte pellets were perfectly dried by suction and stored at −80°C. Metabolites were extracted from the rat primary cultured astrocytes by adding 100 μl cold methanol:water (7:3), containing GABA d_2 (final concentration of 0.5 ppm) as an internal standard. The samples were lysed by performing three cycles of freeze-thaw using liquid nitrogen, and the samples were vortexed for 30 s and then centrifuged at 20 817*g* (14 000 rpm) for 10 min. The supernatant was dried with nitrogen gas using Turbovap LV (Biotage). The samples were then reconstituted with the mobile phase consisting of 80% A and 20% B. The samples were analysed using a UPLC-MS/MS instrument consisting of an ExionLC AD system (AB Sciex) and a triple-quadrupole 4500 mass spectrometer (AB Sciex) equipped with an electrospray ionization source. An Acquity UPLC® BEH HILIC column (2.1 mm × 100 mm, 1.7 μm, Waters) was used to separate the metabolites with the mobile phase A (0.1% formic acid in acetonitrile) and B (0.1% formic acid and 50 mM ammonium formate in water). The flow rate was set to 0.4 ml/min and the injection volume was 5 μl with the following gradient program: starting at 20% B, was maintained for 7 min, and a linear gradient was initiated to reach 80% B over 30 s, then maintained for 1 min, then decreased to 20% B over 30 s and maintained at 20% for 1 min. The total run time was 10 min.

The mass spectrometer was operated in positive ion multiple reaction monitoring (MRM) mode with the following parameters: curtain gas (CUR) at a pressure of 30 psi, turbo IonSpray voltage (IS) at 5500 V, source temperature (TEM) at 550°C, declustering potentials (DP) at 26 V, entrance potentials (EP) at 10 V, collision energies (CE) at 15 V, collision cell exit potential (CXP) at 8 V. Data acquisition was processed using the Analyst® Software (AB Sciex).

RNA sequencing

Total RNA was extracted from the samples using Qiagen RNeasy Mini Kit (#74104, Qiagen). Total RNA (10 μg) was used to prepare sample libraries using Ultra RNA library prep kit (#E7530, NEBNEXT), Multiplex Oligos for Illumina (#E7335, NEBNEXT) and Dynabeads mRNA DIRECT Purification Kit (#61011, Invitrogen) according to the manufacturer's instructions. Full details of the library preparation and sequencing protocol are provided on the website (https://international.neb.com/products/e7530-nebnext-ultra-rna-library-prep-kit-forillumina#Product%20Information). The Agilent 2100 Bioanalyzer (Agilent Technologies) and the associated High Sensitivity DNA kit (Agilent Technologies) were used to determine quality and concentration of the libraries. Sample libraries for sequencing were prepared by the HiSeq Reagent Kit Preparation Guide (Illumina) as described by the manufacturer. Briefly, the combined sample library was diluted to 2 nM, denatured with 0.1 N fresh NaOH, diluted to 20 pM by addition of Illumina HT1 buffer. The library mixture (500 μl) was loaded with Read 1, Read 2 and index sequencing primers on a 206-cycle (2 × 100 paired ends) reagent cartridge (HiSeq reagent kit, Illumina), and run on a HiSeq NEXT generation high-throughput sequencer (Illumina). After the 2 × 100 bp Illumina HiSeq paired-end sequencing run, the data was provided in the form of binary base call (BCL) files. were base called and reads with the same barcode were collected and assigned to a sample on the instrument, which generated Illumina FASTQ files.

For analysis, BCL files obtained from Illumina HiSeq2500 were demultiplexed based on index primer sequences and reads with the same barcode were collected and assigned to a sample, converting them to fastq files. The data were imported to Partek Genomics Suite (Flow ver. 10.0.21.0328; Copyright 2009, Partek Inc.), where further processing was carried out. Briefly, read quality was checked for each sample using FastQC. High-quality reads were aligned using STAR (2.7.3a). Aligned reads were quantified to the mouse genome assembly (mm10, RefSeq Transcripts 93) and normalized to the counts per million (CPM) for inter-sample comparison. Z-scores were calculated from these values and used to prepare heat maps for comparative gene expression visualization.

Autoradiography

APP/PS1 (7–14 months old), 10–11 month old 5xFAD mice and their age-matched wild-type (WT) littermates (three to four mice per each group) were intravenously injected with 5 μCi ^{14}C-acetate ([1, 2-^{14}C]-acetic acid, sodium salt, 115 mCi/mmol, Moravek) or 5 μCi ^{14}C-DG ([1-^{14}C]-2-deoxy-D-glucose, 55 mCi/mmol, conc. 0.1 mCi/ml

in water, American Radiolabeled Chemicals) in 200 μl of saline through the tail vein in 200 μl of saline and perfused with 4% PFA at 1 h post-injection of tracers, respectively. The brains were quickly removed and frozen. For autoradiography, coronal sections (20-μm thickness) were prepared using a cryostat at −20°C and mounted on poly-L-lysine-coated slides. The sections were exposed to an imaging plate (BAS-IP SR2025, FujiFilm) for 2 weeks. The plates were visualized using a bio-imaging analyser system (Typhoon FLA 7000, GE Healthcare). The intensity of radioactivity in the neocortex and hippocampus was quantified using imageJ (NIH). The intensity was normalized with the intensity in the midbrain for ^{14}C-acetate, because the transgenic mice showed lowest amyloid plaque deposition in the midbrain and the ^{14}C-acetate uptake was uniformly low in this brain region. The cerebellum was used as a reference region for ^{14}C-DG, as previously demonstrated. For assessing the age-dependent difference in ^{14}C-acetate uptake, 7-month-old and 12-month-old APP/PS1 mice and the age-matched WT littermates (three mice for each group) were used.

Double staining immunohistochemistry for the human post-mortem brain

Neuropathological examination of normal subject and AD human brain samples was determined using procedures previously established by the Boston University Alzheimer's Disease Center (BUADC). Next of kin provided informed consent for participation and brain donation. Institutional review board approval for ethical permission was obtained through the BUADC centre. This study was reviewed by the Institutional Review Board of the Boston University School of Medicine (Protocol H-28974) and was approved for exemption because it only included tissues collected from post-mortem subjects. The study was performed in accordance with institutional regulatory guidelines and principles of human subject protection in the Declaration of Helsinki. The sample information is listed in Supplementary Table 1.

First staining

Paraffin-embedded tissues were sectioned in a coronal plane at 10 to 20 mm. Endogenous alkaline phosphatase was blocked using 3% hydrogen peroxide in TBS. Sections were blocked with 2.5% normal horse serum (Vector Laboratories) for 1 h and then incubated with MCT1- or GLUT3-specific antibody for 24 h. After washing, sections were incubated with ImmPRESS-AP anti-rabbit IgG (alkaline phosphatase) polymer detection reagent (MP-5402, Vector Laboratories) for 30 min at room temperature. MCT1 signals were developed with a Vector Red alkaline phosphatase substrate kit (Vector Laboratories). GLUT3 signals were developed with a Vector Blue substrate kit (SK-5300, Vector Laboratories).

Second staining

To verify the localization of MCT1 in reactive astrocytes, mouse monoclonal antibody to GFAP (1:200 dilution; Santa Cruz Biotechnology) was incubated over the MCT1-stained tissue slides for 24 h. After washing three times with PBS, the slides were processed with Vector ABC Kit (Vector Laboratories). The GFAP immunoreactive signals were developed with DAB chromogen (Thermo Fisher Scientific). Otherwise, GLUT3-stained slides were subsequently counterstained with Vector Nuclear Fast Red (H-3403, Vector Laboratories). Double-stained tissue slides were processed back to xylene through an increasing ethanol gradient [70%, 80%, and 95% (once), and 100% (twice)] and then mounted.

Human PET imaging

Eleven patients were clinically diagnosed with AD who presented at the dementia outpatient clinic of Severance Hospital, Yonsei University Health System. AD was diagnosed according to the criteria of the National Institute of Neurological and Communicative Disorders and Stroke and the Alzheimer's Disease and Related Disorders Association (NINCDS-ADRDA)[27] and the guideline proposed by Petersen and colleagues.[28] Ten subjects, who had no previous history of neurological disorders or subjective symptoms of cognitive impairment, were selected for normal control (Control). For dynamic analysis study, four patients were clinically diagnosed with AD and one subject was selected for normal control, as described above.

All human subjects underwent neuropsychological testing (Seoul Neuropsychological Screening Battery, SNSB), brain MRI and ^{18}F-FDG, ^{18}F-florbetaben (FBB) and ^{11}C-acetate PET. This study was approved by the institutional review board of Severance Hospital (IRB No. 4-2018-1070), and written informed consent was obtained from all participants. All patients fasted at least 6 h prior to ^{11}C-acetate and ^{18}F-FDG PET scans, which were performed using Discovery 600 (General Electric Healthcare). ^{18}F-FBB was injected at a dose of 300 MBq (8.1 mCi). A dose of 740 MBq (20 mCi) of ^{11}C-acetate was intravenously administered to the patients. For the ^{18}F-FDG PET scan, 4.1 MBq (0.11 mCi) per body weight (kg) of ^{18}F-FDG was intravenously administered to the patients. After the 20 min of uptake period for ^{11}C-acetate, 90 min for ^{18}F-FBB, and 40 min for ^{18}F-FDG, PET scans were performed. The scan time of ^{11}C-acetate, ^{18}F-FBB and ^{18}F-FDG were 20 min, 20 min and 15 min, respectively. The information of CT scan for attenuation correction was following: 0.5 s rotation time, 200 mA, 120 kVp, 3.75 mm section thickness, 10.0 mm collimation, and 9.375 mm table feed per rotation. The acquired PET data were reconstructed using the OSEM with two iterations and 32 subsets.

Prior to the study described above, we performed a pilot study to establish the PET imaging protocol of ^{11}C-acetate in the brain with a normal control subject and four AD patients (Supplementary Fig. 6M). We analysed the distribution volume ratio (DVR) and time-dependent retention of ^{11}C-acetate in the brains of these participants. Each subject was injected with about 20 mCi ^{11}C-acetate as a rapid bolus with simultaneous initiation of a 60-min, 50-frame dynamic acquisition (24 × 5 s, 6 × 10 s, 3 × 20 s, 2 × 30 s, 5 × 60 s, 10 × 300 s), as previously reported.[29] For estimation of the DVR, we used Logan graphical analysis and the reference tissue model. Motor cortex was selected as the reference tissue since ^{11}C-acetate uptake was uniformly low for all patients (Supplementary Fig. 7E). Regional time-activity curves were quantified using regions of interest (ROIs) determined from fused T_1-weighted MRI using the FreeSurfer pipeline 6.0. ^{11}C-acetate uptake of entorhinal cortex was normalized by the value of the motor cortex in the normal subject, and four AD patients (Supplementary Fig. 6N). These dynamic analyses of ^{11}C-acetate retention together showed that ^{11}C-acetate retention was stabilized within 10 min after the tracer injection. Moreover, the correlations between ^{11}C-acetate SUVR and DVR at various time points (10–30 min, 20–40 min, and 40–60 min) were estimated. The DVR was best correlated with time point 20–40 min ($R^2 = 0.9478$), indicating that assessment of the ^{11}C-acetate retention at 20–40 min would be an appropriate protocol (Supplementary Fig. 6P).

For ^{18}F-FDG and ^{11}C-acetate PET analysis, we used standardized uptake value ratio (SUVR) in order to compensate for the undesirable differences in blood glucose level, medication, age, gender and diabetes, which could affect FDG and acetate uptake in the

brain. Pons was used for reference region for normalization of FDG uptake based on previous reports and an SUVR map was generated for visualization.[30,31] For ^{11}C-acetate PET analysis, ^{11}C-acetate SUVR map was generated using the primary motor cortex as a reference region. ^{18}F-FBB were normalized to the mean value in the cerebellar cortex. These regional SUVRs of ^{18}F-FBB were then grouped and averaged into composite SUVRs for the frontal, lateral temporal, mesial temporal, parietal and posterior cingulate cortices. ^{18}F-FBB-PET was defined as positive when visual assessment was scored as 2 or 3 on the brain Aβ plaque load (BAPL) scoring system.[32]

Image processing was performed using MATLAB (The Mathworks, Inc.)-based software called Statistical Parametric Mapping (SPM12, Wellcome Trust Centre for Neuroimaging, London). ^{18}F-FDG PET and corresponding T_1-weighted images were co-registered to the ^{11}C-acetate PET using an automatic registration algorithm based on mutual information. The co-registered T_1 images were segmented into grey matter, white matter and CSF using SPM12's segmentation algorithm. ^{11}C-acetate and the co-registered ^{18}F-FDG PET images were normalized for mean counts in the brain within each scan. PET Images fused with MRI were performed and displayed using the ITK-SNAP (http://www.itksnap.org). A semi-quantitative analysis was performed using the FreeSurfer pipeline 6.0 (Massachusetts General Hospital, Harvard Medical School; http://surfer.nmr.mgh.harvard.edu/). T_1-weighted magnetic resonance images were used to segment cortical ROI based on the Desikan-Killiany Atlas. For both ^{11}C-acetate and ^{18}F-FDG PET analysis, SUVs were first calculated as follows: [decay-corrected activity (kBq) per tissue volume (ml)] / [injected activity (kBq) per body mass (g)]. Then SUVRs of ^{11}C-acetate and ^{18}F-FDG were calculated by normalizing the SUVs by the values of the motor cortex and pons, respectively. Finally, the SUVR intensities were used for displaying the PET images of ^{11}C-acetate and ^{18}F-FDG.

Image quantification

Confocal microscopic images were analysed using the ImageJ program (NIH) and Imaris 9 (Bitplane). For measurement of GFAP and MCT1 immunoreactivity in astrocytes, we first threshold the binary GFAP+ image, but not Adeno-GFAP-GFP+ image, to define single astrocytes as ROIs using ImageJ. Then we measured the intensity of GFAP, GABA or MCT1 in every ROI from 8-bit GFAP+ or MCT1+ images. For measurement of astrocytic GABA intensity, we excluded the cells that is overlapped with the neuron-shaped GABA signals from our ROI list for avoiding the possible contamination from neuronal GABA level. For measurement of GFAP+ volume, we made the surface for each GFAP+ cell with GFAP+ images using Imaris, and then we collected the mean intensity values of the volume of each ROI. GFAP, MCT1 and GLUT3 immunoreactivities in human hippocampal tissues were also analysed using the ImageJ program (NIH). In terms of MCT1 intensity of the double staining images from human tissue staining, we quantified the MCT1 fluorescent intensity, which is stained by Vector Red alkaline phosphatase.

Statistical analyses

Statistical analyses were performed using Prism 9 (GraphPad Software, Inc.). Differences between two different groups were analysed with the two-tailed Student's unpaired *t*-test. For assessment of change of a group by a certain intervention, the significance of data was assessed by the two-tailed Student's paired *t*-test. For comparison of multiple groups, one-way ANOVA with Tukey's or Dunnett's multiple comparison test, or two-way ANOVA with Bonferroni's multiple comparison test was assessed. For assessing the correlations between two factors, linear regression was performed and Pearson's correlation coefficient was calculated. For assessing the correlations between three factors, multiple linear regression was performed and the Mini-Mental State Examination (MMSE) score or SNSB (memory) score was chosen as the outcome. The 3D plots were created using Plotly's Python graphing library. The normality of the distribution of each dataset was tested. When the data do not normally distributed we performed appropriate non-parametric tests such as Mann-Whitney test or Kruskal-Wallis ANOVA test. For comparisons of two or multiple groups, we also tested if the variances are statistically different across the groups. If the variance was different, appropriate corrections were applied to the statistical tests. $P < 0.05$ was considered to indicate statistical significance throughout the study. The significance level is represented with asterisks ($^*P < 0.05$, $^{**}P < 0.01$, $^{***}P < 0.001$; ns = not significant). Unless otherwise specified, all data are presented as mean ± standard error of the mean (SEM). No statistical method was used to predetermine sample size. Sample sizes were determined empirically based on our previous experiences or the review of similar experiments in literatures. The numbers of animals used are described in the corresponding figure legends or on each graph. All experiments were done with at least three biological replicates. Experimental groups were balanced in terms of animal age, sex and weight. Animals were genotyped before experiments, and they were all caged together and treated in the same way. Prior to administration of virus injection or drug administration, animals were randomly and evenly allocated to each experimental group. The data analysis of animal experiments was performed by two independent investigators. However, investigators were not blinded to outcome assessments.

Data and code availability

The data and materials that support the findings of this study are available from the corresponding author on reasonable request. The RNA-sequencing data has been deposited in the Gene Expression Omnibus (GEO) repository with GEO accession code GSE228468.

Results

Reactive astrocytes aberrantly uptake acetate through MCT1

The use of acetate in astrocytes has been reported to be attributable to a transport through monocarboxylate transporters (MCTs).[17] Among many subtypes of MCTs, MCT1 is known to be highly expressed in astrocytes[33] to function as an astrocytic lactate transporter.[34] To examine whether MCT1 functions as a major acetate transporter in astrocytes, the liquid scintillation counting of beta-emitting isotopes was conducted using ^{14}C-acetate with primary cultured astrocytes. We found that treatment with SR13800, an MCT1 inhibitor, dose-dependently blocked the ^{14}C-acetate uptake in primary cultured astrocytes (Fig. 1A and Supplementary Fig. 1A). The gene-silencing of MCT1 using shRNA also significantly blocked the ^{14}C-acetate uptake (Fig. 1B). These findings indicate that MCT1 is essential for acetate uptake in astrocytes.

Thereon, we investigated whether and how MCT1 expression and acetate uptake are altered in reactive astrocytes. We first

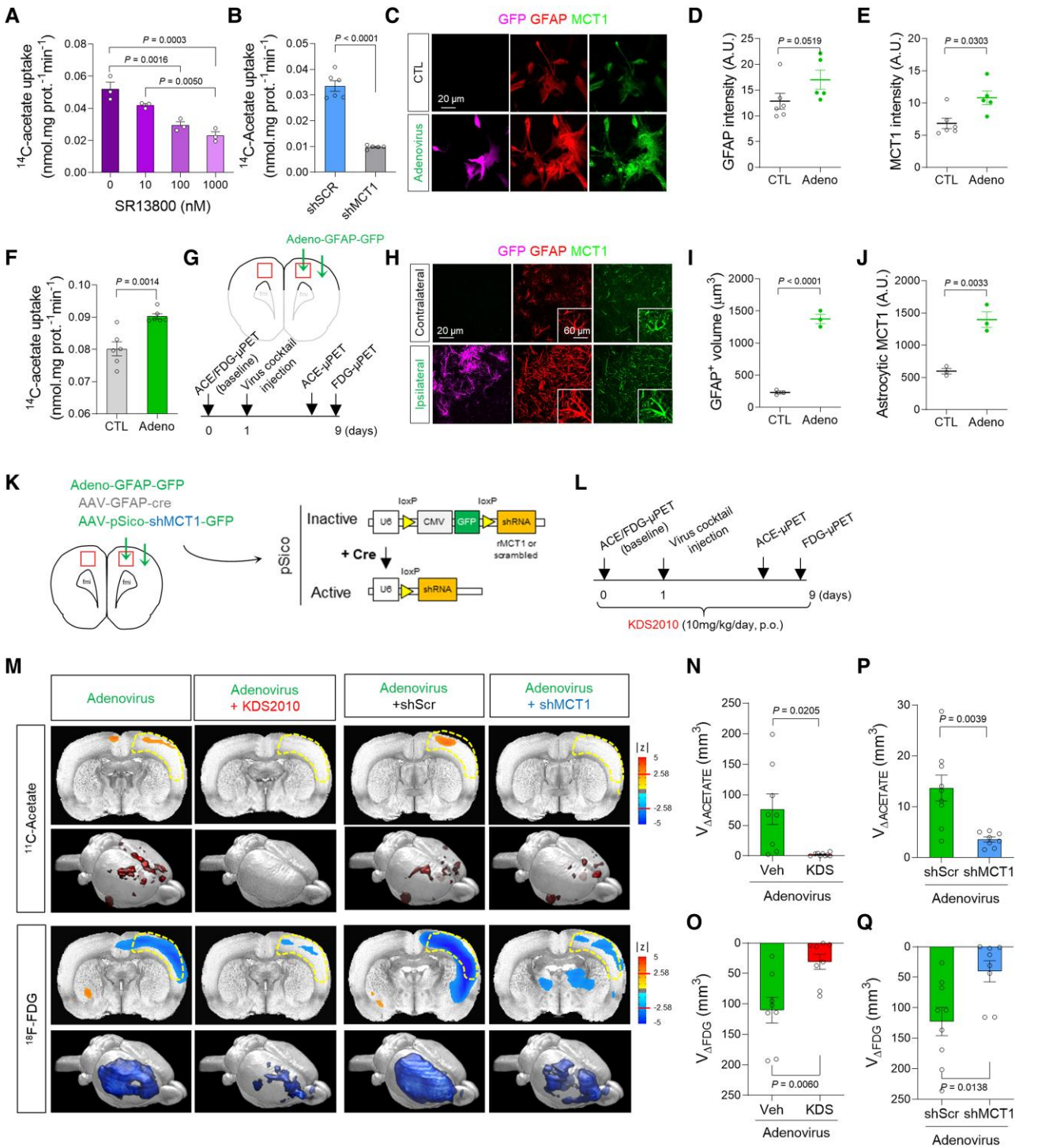

Figure 1 MCT1-mediated acetate hypermetabolism and glucose hypometabolism in the adenovirus-induced reactive astrogliosis model. (**A** and **B**) Blockade effect of SR13800 (**A**) or *Mct1* gene-silencing (**B**) on ^{14}C-acetate uptake in primary cultured astrocytes. (**C**) Representative images displaying GFAP and MCT1 expressions in primary cultured astrocytes 48 h after adenovirus treatment. (**D** and **E**) Quantification of GFAP and MCT1 immunoreactivity ($n = 6$ and 5 replicates for CTL and Adeno groups, respectively). (**F**) The adenovirus effect on ^{14}C-acetate uptake. (**G**) Schematic diagram of *in vivo* micro-PET imaging of adenovirus model. (**H**) Representative images displaying GFAP and MCT1 expressions in adenovirus model. (**I** and **J**) Quantification of the cell volume (**I**) and MCT1 expression (**J**) of GFAP-positive cells ($n = 3$ rats). (**K**) Schematic diagram of virus injection for astrocyte-specific *Mct1* gene-silencing. (**L**) Timeline of PET imaging schedule. (**M**) *Left*: Parametric images from voxel-based comparison of ^{11}C-acetate and ^{18}F-FDG PET imaging in adenovirus model with or without KDS2010 treatment. *Right*: Parametric images from voxel-based comparison of ^{11}C-acetate and ^{18}F-FDG PET imaging in adenovirus model with scrambled-shRNA or MCT1-shRNA. (**N** and **O**) Quantification of the volume of increased ^{11}C-acetate uptake ($n = 8$ and 9 rats for vehicle and KDS2010 groups, respectively). (**P** and **Q**) Quantification of the volume of decreased ^{18}F-FDG uptake ($n = 9$ and 8 rats for shScr and sh*Mct1* groups, respectively). Mean ± SEM. Significance was assessed by one-way ANOVA with Tukey (**A**), Mann-Whitney test (**D**, **E**, **I** and **J**), or two-tailed unpaired Student's *t*-test with Welch's correction (**F**, **N** and **O**) or without Welch's correction (**P** and **Q**).

validated that adenovirus (Adeno-GFAP-GFP) treatment in primary cultured astrocytes induced reactive astrogliosis, as evidenced by increased expressions of GFAP and MAO-B (Fig. 1C and D and Supplementary Fig. 1B), consistent with previous reports.[35] These reactive astrocytes showed a significantly higher MCT1 expression and increased acetate uptake, compared to control astrocytes (Fig. 1E and F). These results are consistent with the previous findings of cytokine-induced reactive astrocytes showing increased MCT1 expression.[36] Two different pro-inflammatory factors using LPS with IFN-γ and Aβ oligomers also increased MCT1 expression in astrocytes, but not in microglia (Supplementary Fig. 1C and D). The increased MCT1 expression in GFAP-positive reactive astrocytes was also observed in an *in vivo* model of reactive astrogliosis induced by unilateral adenovirus injection into the motor and somatosensory cortices of the rat brain[8] (Fig. 1G–J).

Acetate hypermetabolism and glucose hypometabolism in the presence of reactive astrogliosis

To investigate whether acetate metabolism is altered in reactive astrocytes and how it impacts neuronal function *in vivo*, we performed microPET scan using ^{11}C-acetate followed by ^{18}F-FDG with the adenovirus model (Fig. 1K and L). ^{11}C-acetate as a PET tracer has been widely used in clinics for the evaluation of myocardial oxidative metabolism and diagnosis of various non-glycolytic tumours.[37] Meanwhile, only one clinical study has tested the possibility of ^{11}C-acetate in the diagnosis of AD,[38] while its correlation with ^{18}F-FDG uptake has never been explored. We found a significant increase in ^{11}C-acetate uptake and significant decrease in ^{18}F-FDG uptake in the ipsilateral cortex by adenovirus injection, but not in the contralateral cortex (Fig. 1M–O). This finding was consistent with the increased expression of astrocytic MCT1 (Fig. 1H and J and Supplementary Fig. 1E–H) and reduced expression of neuronal glucose transporter 3 (GLUT3) (Supplementary Fig. 1I and J), the main glucose transporter in neurons.[39] These metabolic alterations were prevented by a pharmacological blockade of MAO-B, the key enzyme for inducing reactive astrogliosis,[7,9,10] using a selective and reversible MAO-B inhibitor, KDS2010[10] (Fig. 1M–O). Moreover, the KDS2010 treatment prevented the escalated expression of astrocytic MCT1 in the adenovirus rat model (Supplementary Fig. 1E–H), implying that MCT1 might account for the aberrant acetate uptake. These results indicate that both acetate hypermetabolism and glucose hypometabolism are dependent on MAO-B-mediated reactive astrogliosis.

To investigate if astrocytic MCT1 accounts for adenovirus-induced acetate hypermetabolism, we adopted Cre-LoxP-dependent astrocyte-specific gene-silencing of MCT1 using AAV-GFAP-cre-mCherry and AAV-pSico-rMCT1sh-GFP viruses (Fig. 1K and Supplementary Fig. 2A–F). We found that the astrocytic gene-silencing of MCT1 significantly reduced the adenovirus-induced ^{11}C-acetate uptake, compared to the control scrambled-shRNA (Fig. 1M and P). MCT1 gene-silencing also significantly prevented the adenovirus-induced decrease in ^{18}F-FDG uptake (Fig. 1M and Q), indicating that MCT1 is necessary for both acetate hypermetabolism and glucose hypometabolism. The decrease in ^{18}F-FDG uptake could be attributed to the alterations of neurons, astrocytes, microglia, or all of them, as several recent studies have suggested that astrocytes and microglia could contribute to the ^{18}F-FDG PET signal.[40,41] However, reactive glia reportedly consume more glucose than in their normal states,[42] which was opposite to our observation. Therefore, the decrease in FDG uptake is less likely to be attributable to glial alterations, but more likely to be attributable to the neuronal depression.

Acetate facilitates astrocytic GABA synthesis to reduce neuronal glucose uptake

We have previously demonstrated that the aberrant synthesis and release of GABA from reactive astrocytes cause the neuronal glucose hypometabolism,[8] raising a possibility that the GABA from reactive astrocytes could be responsible for the inverse correlation between acetate and glucose uptake. To test this possibility, we prepared primary cultured cortical astrocytes in glucose-free astrocyte-media supplemented with both putrescine (180 μM), the key substrate for GABA synthesis in astrocytes, and sodium acetate (1 mM). We then assessed the amount of major metabolites in the putrescine-degradation/GABA-synthesis pathway (Fig. 2A) by performing LC-MS with the cultured astrocyte homogenate. We found that putrescine treatment significantly increased the level of N-acetyl-GABA and GABA, only when acetate was supplemented (Fig. 2B–D), indicating the critical role of acetate in boosting astrocytic GABA synthesis via the putrescine degradation pathway. Moreover, astrocyte-specific gene-silencing of MCT1 (Supplementary Fig. 2G–I) significantly reduced the astrocytic GFAP- and GABA-immunoreactivities in the cortex of the adenovirus model (Supplementary Fig. 2J–N). Our RNA sequencing of primary cultured astrocytes with acetate and Aβ treatment further revealed that acetate and Aβ stimulated astrocytic urea cycle and subsequent GABA synthesis, which is consistent with our previous report (Supplementary Fig. 3A–F).[43,44] These results indicate that MCT1-mediated acetate uptake triggers GABA synthesis through the putrescine degradation pathway in astrocytes. A recent report supports our finding by providing evidence that cerebellar astrocytes use ethanol-derived acetate to produce excessive amount of GABA.[45]

We have also previously demonstrated that Aβ treatment causes reactive astrogliosis and exacerbates astrocytic GABA synthesis.[7,10] To assess the role of acetate in Aβ-induced astrocytic GABA synthesis, we performed the sniffer patch technique with GABAc-expressing HEK293T cell as the biosensor (Fig. 2E), as previously described.[26] We found that a 5-day treatment of Aβ (1 μM) turned on GABA synthesis and Ca^{2+}-dependent release, which was significantly increased by the incubation with acetate (10 mM). On the other hand, acetate alone (without Aβ) was not sufficient to turn on the GABA synthesis (Fig. 2F and G), in spite of increased expression of astrocytic GABA-synthesizing enzymes (Supplementary Fig. 3A–E). These findings indicate that the taken-up acetate boosts Aβ-mediated aberrant GABA synthesis in reactive astrocytes. Based on the fact that neuronal glucose uptake can be regulated in an activity-dependent manner (Supplementary Fig. 3F–H),[46,47] the acetate-mediated increase in astrocytic GABA could be responsible for neuronal glucose hypometabolism.

Increased MCT1 and decreased GLUT3 in Alzheimer's disease animal brains

We next asked if the similar metabolic alterations can be recapitulated in animal models of AD, namely including 5xFAD and APP/PS1 mice. We found that MCT1 expression in reactive astrocytes was significantly increased in the cortex of both AD models, compared to WT littermates (Fig. 3A and B and Supplementary Fig. 4A–C). The astrocytic MCT1 expression age dependently increased together with increasing astrocytic reactivity and accumulating Aβ

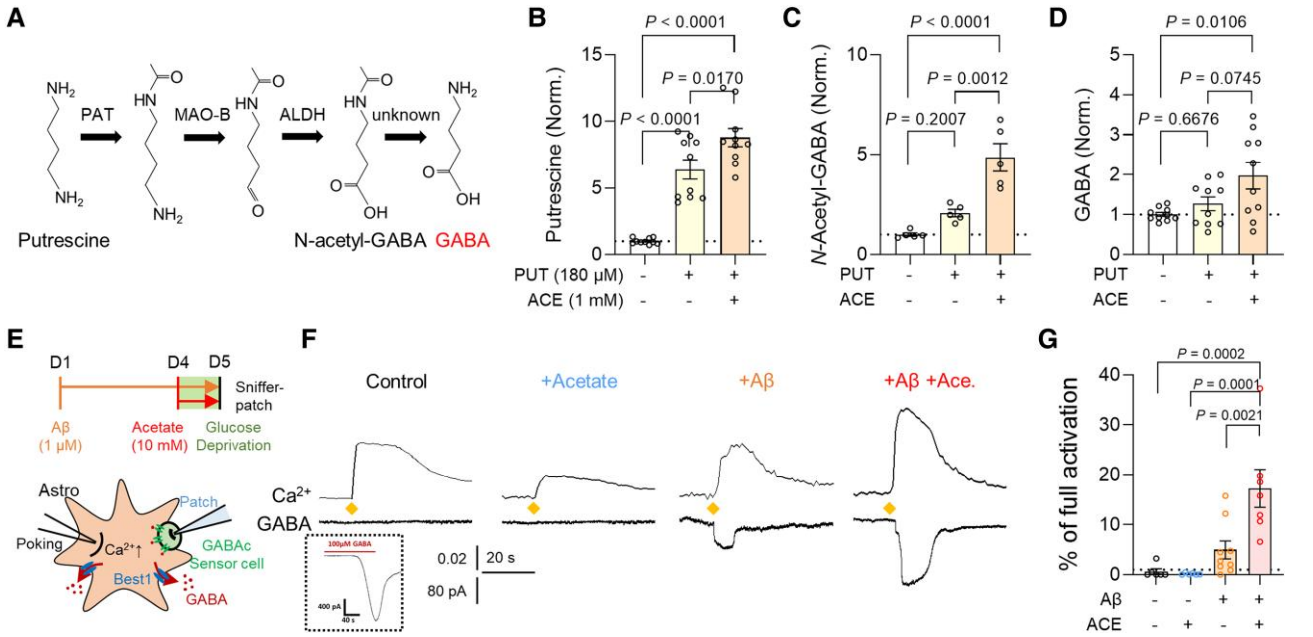

Figure 2 Acetate facilitates astrocytic GABA synthesis in AD-like conditions. (**A**) Schematic diagram of astrocytic GABA-synthetic pathway. (**B–D**) The level of putrescine, *N*-acetyl-GABA and GABA analysed by LC-MS. (**E**) Schematic diagram of sniffer patch to record GABA current. (**F**) Representative traces of Ca^{2+} signal (*top*) and GABA current (*bottom*). Diamonds indicate the time point of poking the astrocyte. (**G**) Quantification of poking-induced GABA current. Mean ± SEM. Significance was assessed by one-way ANOVA with Tukey.

plaques in APP/PS1 mice (Fig. 3H and I). On the other hand, neuronal GLUT3 expression was significantly decreased near the amyloid plaques (Fig. 3C and D and Supplementary Fig. 4D and E). Consistently, acetate uptake was significantly increased while glucose uptake was significantly reduced in the cortex of both 5xFAD and APP/PS1 mice, as revealed by autoradiographs with ^{14}C-acetate and ^{14}C-DG and a ^{14}C-acetate uptake assay (Fig. 3E–G and J and Supplementary Fig. 4J–O). The reduced GLUT3 expression in the APP/PS1 mice was significantly increased by a KDS2010-mediated blockade of astrocytic GABA synthesis (Supplementary Fig. 4F and G). Meanwhile, Aβ-mediated MCT1 increase was not associated with lactate release from cultured astrocytes (Supplementary Fig. 4H and I). These results indicate that acetate hypermetabolism and glucose hypometabolism are closely associated with increased astrocytic MCT1 and decreased neuronal GLUT3 in animal models of AD, respectively. Furthermore, the mechanistic link between MCT1-mediated acetate hypermetabolism and GLUT3-mediated glucose hypometabolism could be GABA, and less likely lactate.

MCT1 critically contributes to astrocytic GABA-mediated Alzheimer's disease pathology

We investigated whether and how astrocytic MCT1 that mediates acetate uptake indeed contributes to AD pathology by adopting a cell type-specific MCT1 gene-silencing strategy (Supplementary Fig. 5A–C). Since we previously reported that MAO-B-mediated astrocytic GABA is critical for AD pathology and memory impairment, we first tested if astrocytic MCT1 expression is critical for astrocytic GABA synthesis and the tonic inhibition of neighbouring hippocampal neurons. Whole-cell patch-clamp recordings and immunohistochemistry demonstrated that MCT1 gene-silencing significantly reduced astrocytic GABA level and tonic inhibition current of hippocampal granule cells in both 5xFAD and APP/PS1 transgenic mice (Fig. 4A and B and Supplementary Fig. 5D–G). On the other hand, astrocytic MCT1 gene-silencing did not alter phasic GABA signalling, as evidenced by unaltered spontaneous inhibitory postsynaptic currents (Fig. 4C–E). Consistent with our previous finding of astrocytic GABA-mediated tonic inhibition suppressing neuronal spike probability, we observed that astrocytic MCT1 gene-silencing restored the electrical stimulation-evoked neuronal spike probability which was reduced in AD mice (Fig. 4F–H and Supplementary Fig. 5H–J). Moreover, astrocytic MCT1 gene-silencing showed a tendency for memory recovery in APP/PS1 transgenic mice (Supplementary Fig. 5K and L). These findings together indicate the necessity of astrocytic MCT1 for aberrant astrocytic GABA synthesis, exacerbated tonic inhibition of hippocampal neurons, and impaired spatial memory in AD model mice.

Increased MCT1 and decreased GLUT3 in Alzheimer's disease human post-mortem brains

To prove our hypothesis in the human pathology, we investigated the protein and mRNA expressions of MCT1 and GLUT3 in post-mortem hippocampal tissues of AD patients and normal subjects (Supplementary Table 1). Consistent with our previous report,[7] we found abundant reactive astrocytes in the brains with AD, as revealed by higher GFAP immunoreactivity (Supplementary Fig. 6A and B). More importantly, we found that MCT1 was highly localized in GFAP-positive astrocytes, and that the astrocytic MCT1 expression was significantly higher throughout the whole hippocampal formation and frontal cortex of AD patients compared to normal subjects (Fig. 5A–G and Supplementary Fig. 6C and D). MCT1 mRNA level was also significantly higher in AD patients than in control subjects (Supplementary Fig. 6E). In contrast, mRNA and protein expressions of GLUT3 in neurons was significantly decreased in AD (Fig. 5H–L and Supplementary Fig. 6F–L), whereas mRNA expression of GLUT1 was not altered in AD

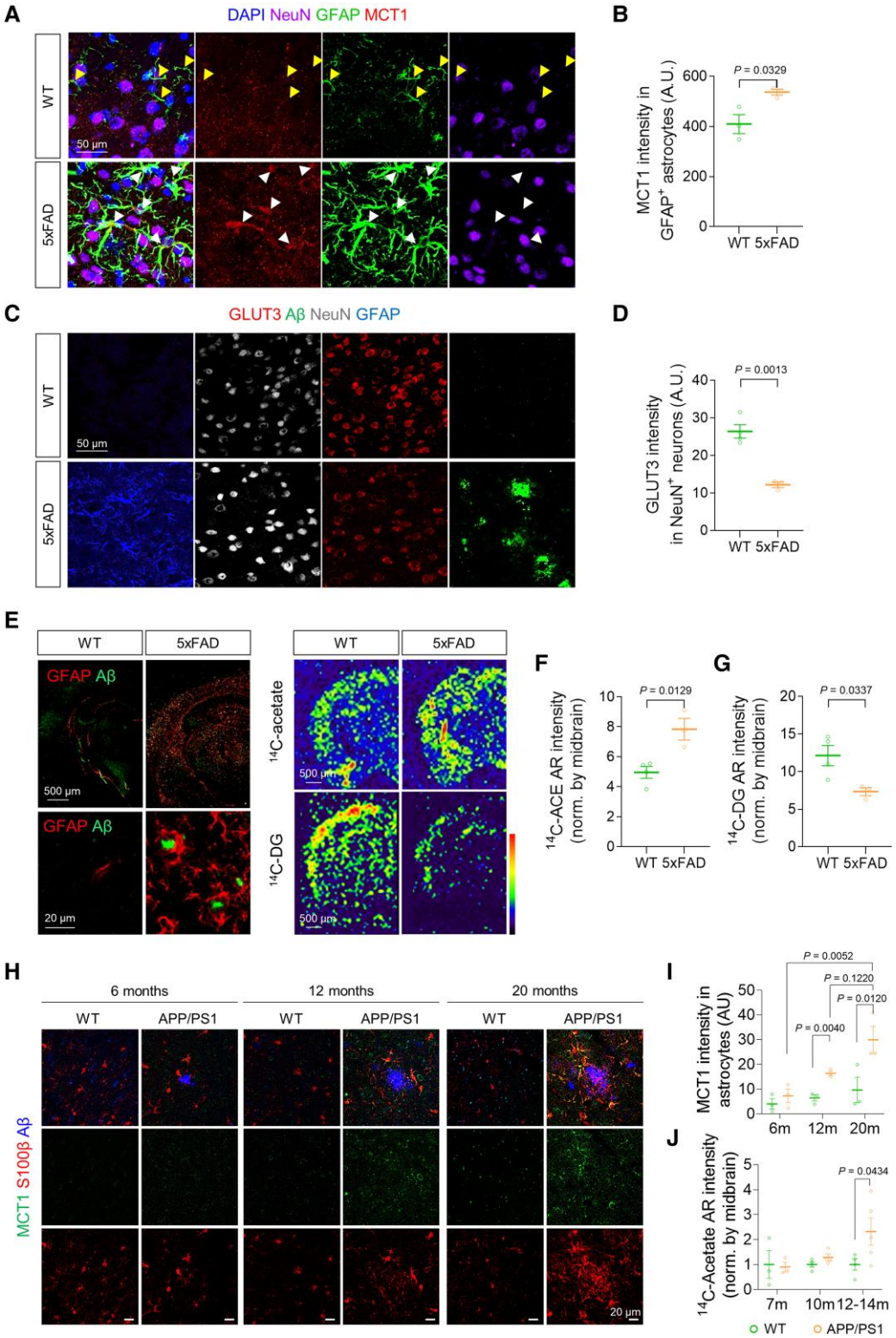

Figure 3 Increased MCT1 and reduced GLUT3 are associated with acetate hypermetabolism and glucose hypometabolism in AD mice. (**A**) Representative images displaying GFAP and MCT1 expressions in the cortex of 5xFAD mice. (**B**) Quantification of astrocytic MCT1 immunoreactivity ($n = 3$ mice for each group). (**C**) Representative images displaying NeuN and GLUT3 expressions in the cortex of 5xFAD mice. (**D**) Quantification of neuronal GLUT3 immunoreactivity ($n = 3$ mice for each group). (**E**) *Top*: Representative images displaying Aβ-plaque and GFAP expressions in 5xFAD mice. *Bottom*: Representative autoradiographic images of ^{14}C-acetate and ^{14}C-DG. (**F** and **G**) Quantification of ^{14}C-acetate and ^{14}C-DG ($n = 4$ and 3 mice for WT and 5xFAD, respectively). (**H**) Representative confocal images of MCT1 and S100b in 6-, 12- and 20-month-old (m) APP/PS1 transgenic mice. (**I**) Quantification of S100b-positive astrocytic MCT1 expression ($n = 3$ for each group). (**J**) Quantification of ^{14}C intensity ($n = 3$, 3, 4, 4, 4 and 5 mice for 7 m WT, 7 m APP/PS1, 10 m WT, 10 m APP/PS1, 12–14 m WT, and 12–14 m APP/PS1, respectively). Mean ± SEM for bar graphs. Median and quartiles for violin plots. Significance was assessed by two-tailed unpaired Student's *t*-test (**B**, **D**, **F** and **G**), Two-way ANOVA with Tukey (**I**), or Two-way ANOVA with Sidak (**J**).

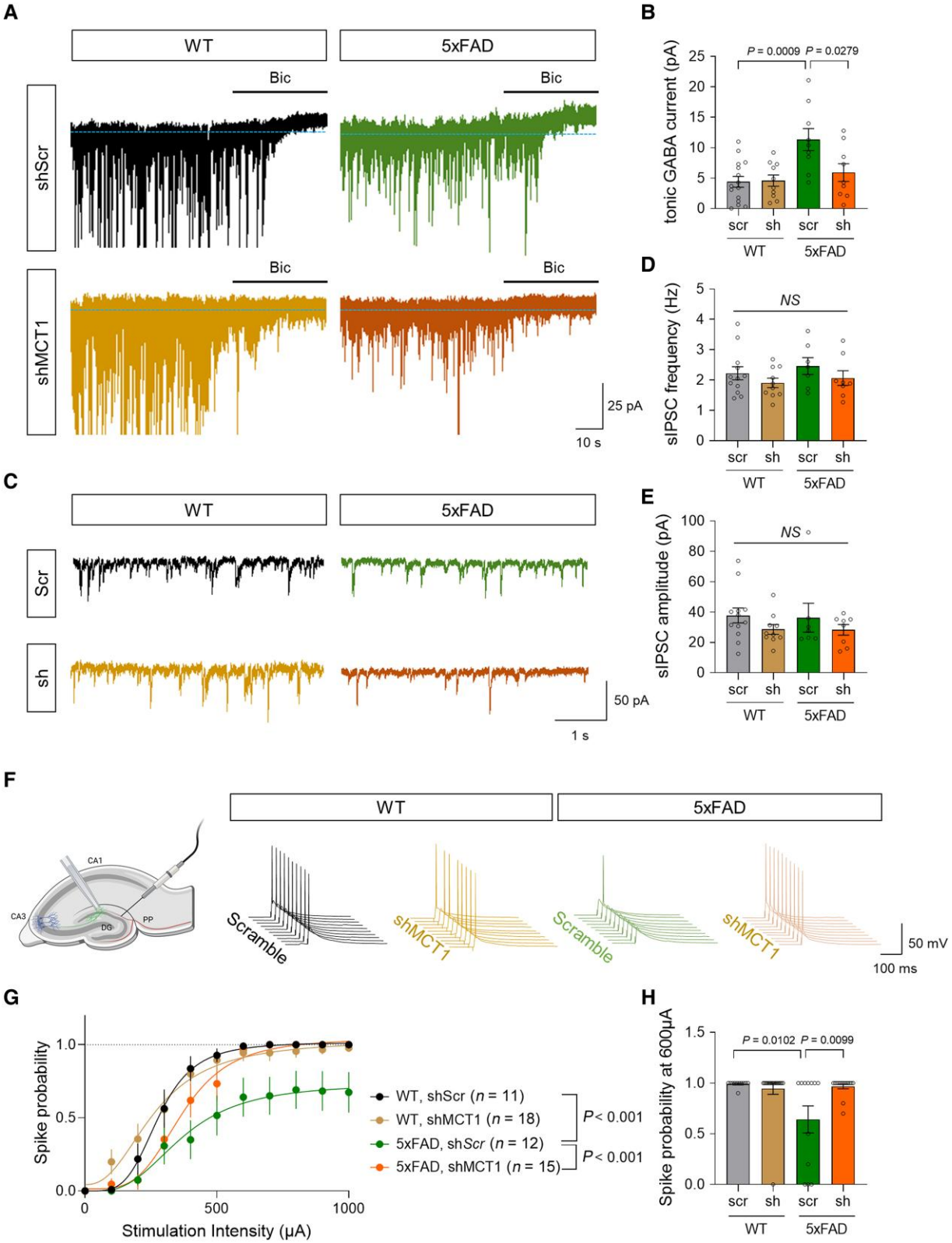

Figure 4 Astrocytic MCT1 gene-silencing reduces tonic inhibition and spike probability in the hippocampus of an AD mouse model. (**A**) Representative traces of tonic GABA recording from hippocampal dentate granule cells of 5xFAD and WT littermates. (**B**) Quantification of tonic GABA current ($n = 15$, 10, 9 and 9 cells from three mice for each group). (**C**) Representative traces of spontaneous inhibitory postsynaptic current (sIPSC) recording. (**D** and **E**) Quantification of sIPSC frequency and amplitude ($n = 12$, 10, 7 and 8 cells from three mice for each group). (**F**) Schematic diagram of action potential recording from dentate granule cells upon electrical stimulation of hippocampal perforant path (*left*) and representative traces of spike probability. (**G**) Quantification of spike probability upon various stimulation intensities ($n = 11$, 18, 12 and 15 cells from three mice for each group). (**H**) Quantification of spike probability at 600 μA stimulation. Mean ± SEM. Significance was assessed by one-way ANOVA with Tukey.

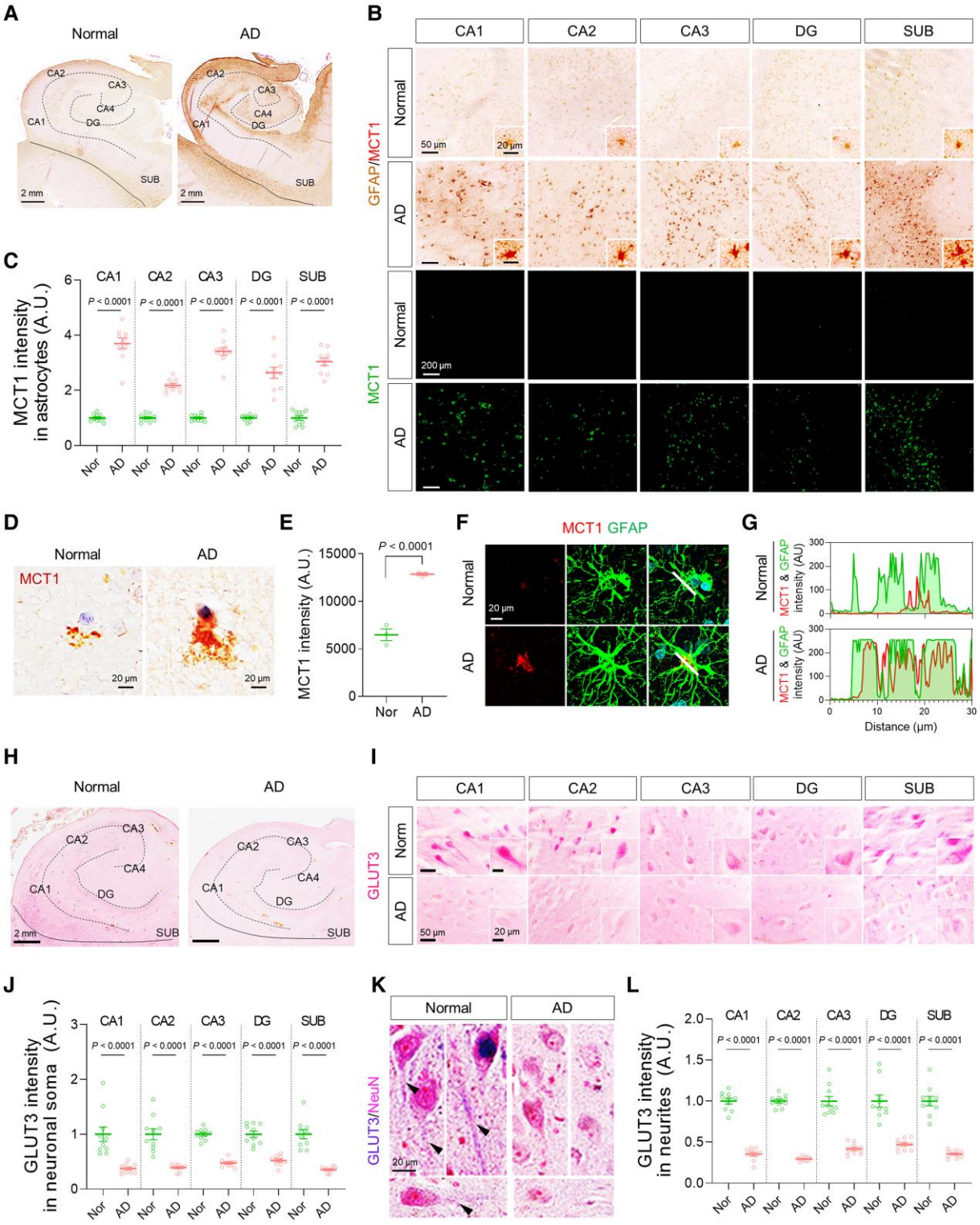

Figure 5 Astrocytic MCT1 is increased while neuronal GLUT3 is decreased in the hippocampus of AD patients. (**A** and **B**) Representative images of double-staining of GFAP and MCT1 in post-mortem hippocampal tissues from normal subjects ($n = 10$) and AD post-mortem brains ($n = 10$). (**C**) Quantification of astrocytic MCT1 intensity in each hippocampal sub-region. (**D**) Representative images of MCT1 immunoreactivity in the cortex of normal subject and AD patient. (**E**) Quantification of MCT1 intensity in the cortex of normal subjects ($n = 3$) and AD patients ($n = 3$). (**F**) Representative images of double-staining of MCT1 (red) and GFAP (green) in the cortex of normal subject and AD patient. (**G**) Co-localization analysis of MCT1 and GFAP signals in the cortex of normal subject and AD patient. White lines in merged images were drawn to measure the space cross-correlation of MCT1 and GFAP signals. (**H** and **I**) Representative images of single-staining of GLUT3 in neuronal soma of post-mortem hippocampal tissues from normal subjects ($n = 10$) and AD post-mortem brains ($n = 10$). (**J**) Quantification of GLUT3 intensity in neuronal soma. (**K**) Representative images of double-staining of NeuN and GLUT3 in neurites. (**L**) Quantification of GLUT3 intensity in neurites. Mean ± SEM. Significance was assessed by two-tailed unpaired Student's *t*-test (**E**), Mann-Whitney test (**J**, CA1, CA2, DG and SUB; **L**, SUB) or two-tailed unpaired Student's *t*-test with Welch's correction (others).

(Supplementary Fig. 6I). The reduced GLUT3 expression could be attributed to both astrocyte-mediated neuronal metabolic depression and neurodegeneration. These results indicate that MCT1 is increased in reactive astrocytes and GLUT3 is reduced in the neighbouring neurons, suggesting the feasibility of using ^{11}C-acetate and ^{18}F-FDG PET imaging in AD patients.

Astrocytic acetate hypermetabolism correlates with cognitive decline in Alzheimer's disease patients

To examine the feasibility, we performed PET imaging with ^{11}C-acetate and ^{18}F-FDG in 11 AD patients (four males and seven females; mean age 74.45 ± 6.79 years) and 10 healthy volunteers (eight males and two females; mean age 69.00 ± 10.49 years) (Supplementary Fig. 6M). All participants underwent MRI and ^{18}F-florbetaben (FBB) PET scans after their initial clinical examinations (Supplementary Fig. 6N and O and Supplementary Tables 2 and 3). Since ^{11}C-acetate has rarely been used in AD patients, we validated our imaging protocol which involved assessing the ^{11}C-acetate retention within 20–40 min after the tracer injection by performing dynamic analyses of ^{11}C-acetate retention (Supplementary Fig. 7A–E). Subsequently, a semi-quantitative analysis of individual PET data was performed in the brain regions implicated in Braak stages of AD, including the entorhinal cortex, hippocampus, fusiform, inferior, middle and superior temporal gyrus (Fig. 6A and B). We found that the SUVR on ^{11}C-acetate PET was significantly higher in all the regions of AD brains (Fig. 6C), while the SUVR on ^{18}F-FDG PET had significantly decreased (Fig. 6D). The ^{11}C-acetate SUVR and ^{18}F-FDG SUVR showed distinct inverse correlations particularly in the entorhinal cortex and hippocampus (Fig. 6E). In addition, we could observe significant increased ^{11}C-acetate PET uptake and reduced ^{18}F-FDG PET in angular, supramarginal, posterior cingulate gyrus and prefrontal cortex, which are known to exhibit heavy Aβ deposits, thereby provoking reactive astrogliosis (Supplementary Fig. 7F and G). On the other hand, we could not observe any significant alteration in either ^{11}C-acetate or ^{18}F-FDG uptake of the cerebellar cortex, which is one of the least affected brain regions by AD pathology (Supplementary Fig. 7F and G).

Furthermore, we analysed the multiple correlations among ^{11}C-acetate uptake, ^{18}F-FDG uptake and cognitive function. We first found that SUVR of ^{11}C-acetate in each brain region showed significant and strong correlation with either the Korean-MMSE (K-MMSE) score (Fig. 6E and Supplementary Fig. 8B) or memory score of the SNSB (Supplementary Fig. 8C). Similar high correlations were observed in the SUVR of ^{18}F-FDG (Supplementary Fig. 8A). Finally, multiple linear regression showed that MMSE scores highly correlated with both ^{11}C-acetate SUVR and ^{18}F-FDG SUVR with the highest R^2 values in the entorhinal cortex and hippocampus (Fig. 6F and Supplementary Fig. 8B). Taken together, these results indicate the reactive astrogliosis visualized by ^{11}C-acetate and the associated neuronal dysfunction visualized by ^{18}F-FDG to be highly correlated with cognitive impairment for AD patients. Furthermore, our findings provide the first *in vivo* evidence for the critical role of reactive astrogliosis in human AD symptomatology, which has been suspected for several decades based on animal studies.

Discussion

A key highlight of our study is that PET imaging in combination with ^{11}C-acetate and ^{18}F-FDG can visualize the reactive astrocyte-neuron interaction in AD patients. While ^{18}F-FDG have been used for the diagnosis of AD combined with amyloid PET imaging, ^{11}C-acetate has much less been similarly considered. ^{11}C-acetate has two distinct merits in clinical use. First, acetate is an abundantly ubiquitous molecule in the body, which guarantees its safety for clinical application. Second, ^{11}C isotopes quickly decay due to their short half-life, which allow dual PET imaging with various ^{18}F-labelled tracers. Another highlight was that we delineated the molecular and cellular mechanisms of acetate hypermetabolism and glucose hypometabolism in AD by identifying the key molecular targets of astrocytic MCT1 for acetate uptake, and neuronal GLUT3 for glucose uptake. Particularly, we have re-evaluated the function of MCT1 as an astrocytic acetate transporter, while it has been previously reported as a lactate transporter.[48] Through *in vitro* and animal experiments, we demonstrated that reactive astrocytes show high MCT1 expression and excessive acetate uptake. The taken-up acetate could facilitate the synthesis of astrocytic GABA which inhibits the neighbouring neuronal activity, which could be associated with the GLUT3-mediated glucose uptake (Supplementary Fig. 9). Intriguingly, the reactive astrocyte-mediated acetate metabolism (revealed by ^{11}C-acetate SUVR) and the associated neuronal hypometabolism (revealed by ^{18}F-FDG SUVR) highly correlated with the cognitive decline of AD patients. Our results together indicate that the acetate-boosted reactive astrocyte-neuron interaction could be important for neuronal dysfunction and the associated cognitive decline. Furthermore, these findings raise a possibility that reactive astrogliosis leading to neuronal hypometabolism could be an effective imaging target for AD patients.

^{11}C-acetate has been proposed as a PET tracer for astrocyte metabolism from a long time,[49] but has rarely been used in patients with neurodegenerative diseases. This might be due to the misconception that ^{11}C-acetate would be entirely converted into labelled CO_2 and quickly disappear from the brain. On the contrary, it has been reported that radiolabelled acetate could be also used for the synthesis of several metabolites including glutamate, glutamine and GABA.[45,49] Furthermore, previous kinetic modelling studies showed a rapid synthesis and clearance of ^{11}C-CO_2 within 10 min after ^{11}C-acetate injection and the brain ^{11}C-radioactivity remained fairly constant throughout 60 min.[29,38] The steady-state ^{11}C-radioactivity could also be affected by changes in the amounts and activities of not only MCT1, but enzymes catalysing the acetate metabolism as well, along with the blood perfusion and blood–brain barrier integrity. In the current study, we successfully demonstrated the increased ^{11}C-acetate retention in reactive astrocytes of the AD patients' brain scans by PET imaging after 20 min of ^{11}C-acetate administration. Consistently, several recent studies have reported the increased ^{11}C-acetate retention in patients of multiple sclerosis[22,29] and glioblastoma,[50,51] accompanying reactive astrogliosis. Moreover, ^{11}C-acetate has an advantage of fast decaying which allows simultaneous imaging with other ^{18}F-labelled tracers. Taken together, ^{11}C-acetate PET imaging together with ^{18}F-FDG PET imaging provides a proof-of-concept of acetate-boosted reactive astrocyte-neuron interaction in the brains of AD patients when the PET signals are acquired following the first 20 min.

Our study demonstrates that reactive astrocytes aberrantly absorb acetate in the affected brain regions of both AD patients and animal models, which in turn boosts GABA synthesis. The detailed mechanism of how acetate facilitates GABA synthesis is unclear, but it could be attributed to an increased acetylation of spermine and spermidine by acetate-originated acetyl-CoA, causing overproduction of putrescine,[52,53] the precursor metabolite of GABA. This putrescine accumulation leading to GABA production in astrocytes causes substantial changes in nearby neurons, as well. As we

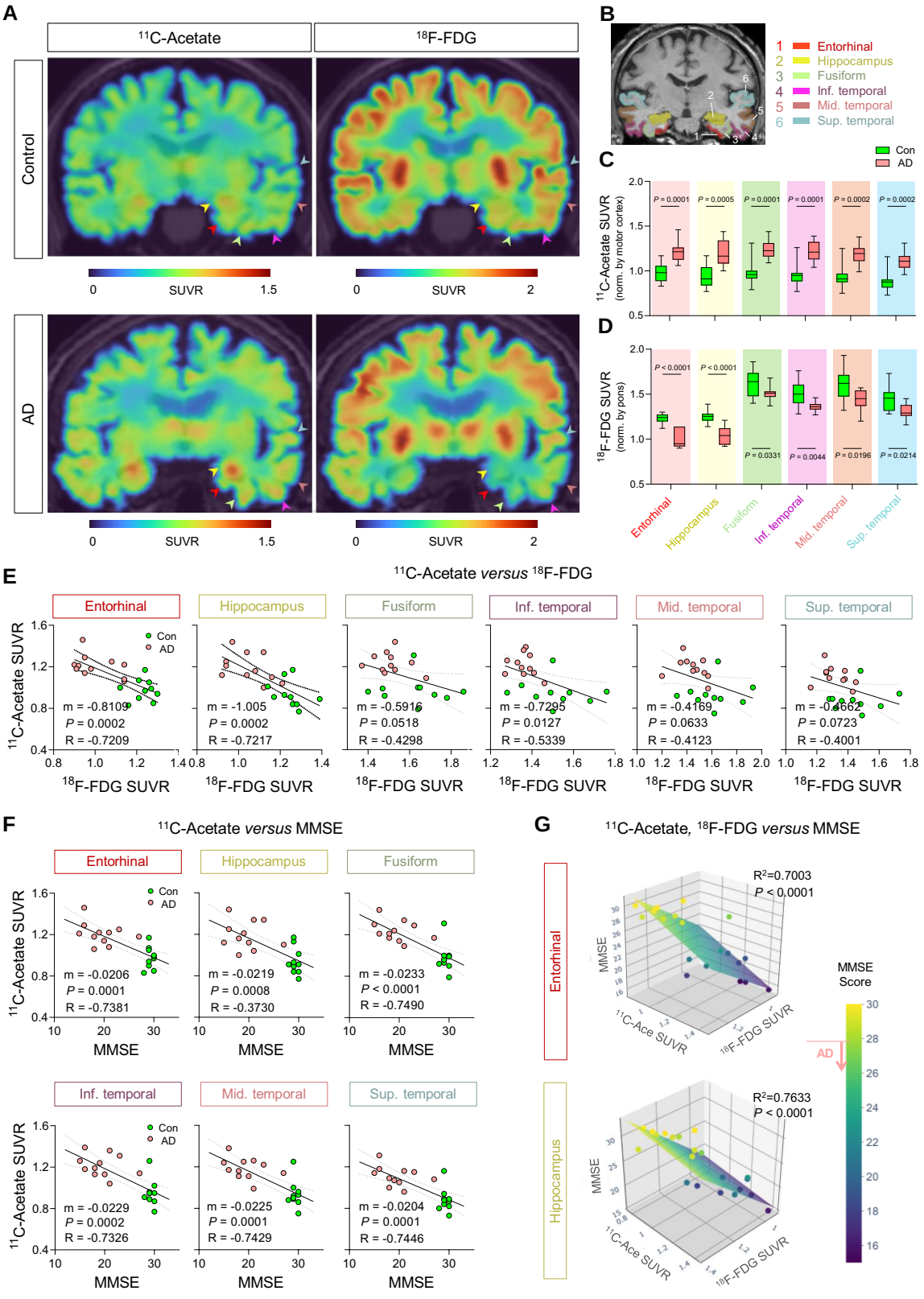

Figure 6 ^{11}C-acetate and ^{18}F-FDG PET imaging for visualizing reactive astrogliosis and the associated neuronal glucose hypometabolism in AD patients' brains. (**A**) Representative PET images of ^{11}C-acetate and ^{18}F-FDG in control and AD patients. (**B**) ROIs from an MR image. The ROI colours are matched with arrowheads in **A**. (**C** and **D**) Quantification of ^{11}C-acetate and ^{18}F-FDG SUVR in each ROI of control ($n = 10$) and AD patients ($n = 11$). (**E**) Correlation between ^{11}C-acetate SUVR and MMSE scores. (**F**) Multiple correlations between ^{11}C-acetate SUVR, ^{18}F-FDG SUVR in entorhinal cortex and hippocampus, and MMSE scores. The multiple correlations in the fusiform, inferior, middle and superior temporal gyrus are displayed in Supplementary Fig. 7B. Mean ± SEM. Significance was assessed by two-tailed unpaired Student's *t*-test (**C** and **D**), linear regression (**E**), or multiple linear regression (**F**) with Pearson's correlation.

have previously reported, astrocytic GABA-mediated tonic inhibition suppressed neuronal glucose uptake in a subcortical stroke model.[8] Consistently, it has been demonstrated that extrasynaptic $GABA_A$ receptor-mediated signalling bidirectionally regulates the ^{18}F-FDG uptake in the brain.[54] In this study, we also observed that decreased ^{18}F-FDG uptake coincided with increased ^{11}C-acetate uptake. These lines of evidence support the idea that astrocytic acetate hypermetabolism causing aberrant synthesis of GABA, in addition to loss of neurons and synapses, leads to reduced glucose metabolism in neighbouring neurons. Taken together, the increased astrocytic acetate metabolism causes a cascade of events leading to neuronal glucose hypometabolism, allowing the PET imaging with ^{11}C-acetate and ^{18}F-FDG to visualize the pathological astrocyte-neuron interaction in the living human brains of AD patients. This could be extended to a universal mechanism of neuroinflammation in various brain diseases including AD, dementia with Lewy bodies (Supplementary Fig. 10A), Parkinson's disease (Supplementary Fig. 10B–F), multiple sclerosis,[22,29] and glioblastoma.[44]

The increased acetate uptake in the AD brains could be attributed to either the increased expression of the acetate transporter, MCT1, increased extracellular acetate level in the brain, or both. The first possibility has been proved by our finding that astrocytic MCT1 expression was significantly increased in the brains of AD model mice and the patients. The increased MCT1 expression and the excessive demand on acetate could be attributed to the reactivity of astrocytes, which is elicited by digesting misfolded proteins such as Aβ oligomers.[43] The next possibility is the alteration in extracellular acetate levels in the brain. If the brain acetate concentration is increased, it could firstly be attributed to increased acetate synthesis in the gut microbiota which can affect AD pathology.[55,56] Second, it could be attributed to increased acetate synthesis from activated microglia which vigorously consume glucose for glycolysis under inflammatory conditions.[41] Similarly, it has been reported that glioblastoma aberrantly takes up glucose and excessively releases acetate.[44] These interesting possibilities about whether and how acetate concentration is increased in the AD brains should be investigated in future studies.

Even though we investigated the possible role of acetate in AD pathology and the potential diagnostic value of simultaneous PET imaging with ^{11}C-acetate and ^{18}F-FDG, our study might have several limitations. First, the small sample size of our human PET imaging study limits the generalizability of our study. Second, although we demonstrated that MCT1 gene-silencing restored aberrant astrocytic GABA synthesis, tonic inhibition of neurons, and impaired memory function, our study still lacks the direct evidence to determine whether acetate has a detrimental or beneficial action in AD pathology or not. As MCT1 is known to transport not only acetate but lactate and pyruvate as well, genetic manipulation of MCT1 cannot rule out the role of lactate and pyruvate. Moreover, there has been a conflicting result about the beneficial effect of acetate on the pathology of AD model.[57] Therefore, the possible pathological role of acetate in AD deems further investigation.

In the past two decades, several attempts for imaging neuroinflammation have been undertaken by targeting mitochondrial translocator protein (TSPO)[58–60] and MAO-B.[3,12] However, those attempts have been faced with several limitations. Firstly, although microglial TSPO is known to be highly upregulated under neuroinflammatory conditions, TSPO targeting PET has given inconsistent and conflicting results of low and high efficiencies in discriminating AD brains from healthy brains.[61–64] Secondly, the currently available MAO-B-targeting PET tracer, ^{11}C-deuterium-L-deprenyl is derived from L-deprenyl, also known as selegiline, which shows relatively poor selectivity for MAO-B over MAO-A; the IC_{50} for MAO-B is only 150-fold lower than that for MAO-A,[10] raising a possibility that this probe can target MAO-A as well as MAO-B. Meanwhile, recently developed selective and reversible MAO-B tracers such as ^{18}F-SMBT-1 show some promising results to circumvent those limitations.[65,66] Therefore, in combination with ^{18}F-FDG, the selective and reversible MAO-B tracers should be tested for labelling the reactive astrogliosis and the associated neuronal hypometabolism in AD brains.

Current approaches of molecular imaging through brain PET are mostly focused on visualizing the presence of certain molecules or the activity of certain types of neurons. These approaches have failed to provide information on how astrocytes and neurons interact with each other. Our proposed imaging strategy with ^{11}C-acetate and ^{18}F-FDG should be valuable for the simultaneous imaging of reactive astrogliosis and the associated neuronal dysfunction in the living brains of AD patients. Knowing the exact status of reactive astrogliosis should be helpful for realizing a more comprehensive pathophysiology of AD by complementing the conventional PET probes targeting amyloid plaques and tau protein aggregates. Therefore, the future development of various imaging strategies for visualizing the functional interactions between reactive astrocytes and neurons is awaited.

Funding

This study was supported by IBS-R001-D2 from the Institute for Basic Science funded by the Ministry of Science and ICT to C.J.L.; NRF-2018M3C7A1056898 and NRF-2020R1A2B5B01098109 from National Research Foundation (NRF) of Korea to M.Y.; NRF-2018M3C7A1056894, NRF-2020M3E5D9079742, and KIST Grants (2E30320, 2E30762) to H.R.; NRF-2018M3C7A1056897 and KIST Grant (2E32162) to M.-H.N; and P30AG072978 from National Institute of Aging to T.S.

Competing interests

The authors report no competing interests.

Supplementary material

Supplementary material is available at *Brain* online.

References

1. Chun H, Lee CJ. Reactive astrocytes in Alzheimer's disease: A double-edged sword. *Neurosci Res*. 2018;126:44-52.
2. Nordberg A. Molecular imaging in Alzheimer's disease: New perspectives on biomarkers for early diagnosis and drug development. *Alzheimers Res Ther*. 2011;3:34.
3. Carter SF, Scholl M, Almkvist O, *et al*. Evidence for astrocytosis in prodromal Alzheimer disease provided by 11C-deuterium-L -deprenyl: A multitracer PET paradigm combining 11C -Pittsburgh compound B and 18F-FDG. *J Nucl Med*. 2012;53:37-46.
4. Bi F, Huang C, Tong J, *et al*. Reactive astrocytes secrete lcn2 to promote neuron death. *Proc Natl Acad Sci U S A*. 2013;110: 4069-4074.
5. Tao J, Wu H, Lin Q, *et al*. Deletion of astroglial dicer causes non-cell-autonomous neuronal dysfunction and degeneration. *J Neurosci*. 2011;31:8306-8319.
6. Chun H. Severe reactive astrocytes precipitate pathological hallmarks of Alzheimer's disease via excessive H2O2-production. *Nat Neurosci*. 2020;23:1555-1566.

7. Jo S, Yarishkin O, Hwang YJ, *et al*. GABA From reactive astrocytes impairs memory in mouse models of Alzheimer's disease. *Nat Med*. 2014;20:886-896.
8. Nam MH, Cho J, Kwon DH, *et al*. Excessive astrocytic GABA causes cortical hypometabolism and impedes functional recovery after subcortical stroke. *Cell Rep*. 2020;32:107861.
9. Heo JY, Nam MH, Yoon HH, *et al*. Aberrant tonic inhibition of dopaminergic neuronal activity causes motor symptoms in animal models of Parkinson's disease. *Curr Biol*. 2020;30:276-291.e9.
10. Park JH, Ju YH, Choi JW, *et al*. Newly developed reversible MAO-B inhibitor circumvents the shortcomings of irreversible inhibitors in Alzheimer's disease. *Sci Adv*. 2019;5:eaav0316.
11. Chen Z, Zhong C. Decoding Alzheimer's disease from perturbed cerebral glucose metabolism: Implications for diagnostic and therapeutic strategies. *Prog Neurobiol*. 2013;108:21-43.
12. Rodriguez-Vieitez E. PET Imaging of monoamine oxidase B. In: Dierckx RA, Otte A, de Vries EF, van Waarde A, Lammertsma AA, eds. *PET And SPECT of neurobiological systems*. Springer; 2021:521-545:chap 15.
13. Zhang Y, Sloan SA, Clarke LE, *et al*. Purification and characterization of progenitor and mature human astrocytes reveals transcriptional and functional differences with mouse. *Neuron*. 2016;89:37-53.
14. Tong J, Meyer JH, Furukawa Y, *et al*. Distribution of monoamine oxidase proteins in human brain: Implications for brain imaging studies. *J Cereb Blood Flow Metab*. 2013;33:863-871.
15. Tong J, Rathitharan G, Meyer JH, *et al*. Brain monoamine oxidase B and A in human parkinsonian dopamine deficiency disorders. *Brain*. 2017;140:2460-2474.
16. Nicklas WJ, Clarke DD. Decarboxylation studies of glutamate, glutamine, and aspartate from brain labelled with [1-14C]acetate, L-[U-14C]-aspartate, and L-[U-14C]glutamate. *J Neurochem*. 1969;16:549-558.
17. Waniewski RA, Martin DL. Preferential utilization of acetate by astrocytes is attributable to transport. *J Neurosci*. 1998;18:5225-5233.
18. Cruz NF, Lasater A, Zielke HR, Dienel GA. Activation of astrocytes in brain of conscious rats during acoustic stimulation: Acetate utilization in working brain. *J Neurochem*. 2005;92:934-947.
19. Wyss MT, Magistretti PJ, Buck A, Weber B. Labeled acetate as a marker of astrocytic metabolism. *J Cereb Blood Flow Metab*. 2011;31:1668-1674.
20. Rowlands BD, Klugmann M, Rae CD. Acetate metabolism does not reflect astrocytic activity, contributes directly to GABA synthesis, and is increased by silent information regulator 1 activation. *J Neurochem*. 2017;140:903-918.
21. Sancheti H, Patil I, Kanamori K, *et al*. Hypermetabolic state in the 7-month-old triple transgenic mouse model of Alzheimer's disease and the effect of lipoic acid: A 13C-NMR study. *J Cereb Blood Flow Metab*. 2014;34:1749-1760.
22. Takata K, Kato H, Shimosegawa E, *et al*. 11C-acetate PET imaging in patients with multiple sclerosis. *PLoS One*. 2014;9:e111598.
23. Grimm D, Lee JS, Wang L, *et al*. In vitro and in vivo gene therapy vector evolution via multispecies interbreeding and retargeting of adeno-associated viruses. *J Virol*. 2008;82:5887-5911.
24. Cox RW. AFNI: Software for analysis and visualization of functional magnetic resonance neuroimages. *Comput Biomed Res*. 1996;29:162-173.
25. Papp EA, Leergaard TB, Calabrese E, Johnson GA, Bjaalie JG. Waxholm Space atlas of the sprague dawley rat brain. *Neuroimage*. 2014;97:374-386.
26. Oh SJ, Lee JM, Kim HB, *et al*. Ultrasonic neuromodulation via astrocytic TRPA1. *Curr Biol*. 2019;29:3386-3401.e8.
27. McKhann G, Drachman D, Folstein M, Katzman R, Price D, Stadlan EM. Clinical diagnosis of Alzheimer's disease: Report of the NINCDS-ADRDA Work Group under the auspices of Department of Health and Human Services Task Force on Alzheimer's disease. *Neurology*. 1984;34:939-944.
28. Petersen RC, Smith GE, Waring SC, Ivnik RJ, Tangalos EG, Kokmen E. Mild cognitive impairment: Clinical characterization and outcome. *Arch Neurol*. 1999;56:303-308.
29. Kato H, Okuno T, Isohashi K, *et al*. Astrocyte metabolism in multiple sclerosis investigated by 1-C-11 acetate PET. *J Cereb Blood Flow Metab*. 2021;41:369-379.
30. Kim S, Lee P, Oh KT, *et al*. Deep learning-based amyloid PET positivity classification model in the Alzheimer's disease continuum by using 2-[(18)F]FDG PET. *EJNMMI Res*. 2021;11:56.
31. Nugent S, Croteau E, Potvin O, *et al*. Selection of the optimal intensity normalization region for FDG-PET studies of normal aging and Alzheimer's disease. *Sci Rep*. 2020;10:9261.
32. Barthel H, Gertz HJ, Dresel S, *et al*. Cerebral amyloid-beta PET with florbetaben (18F) in patients with Alzheimer's disease and healthy controls: A multicentre phase 2 diagnostic study. *Lancet Neurol*. 2011;10:424-435.
33. Broer S, Rahman B, Pellegri G, *et al*. Comparison of lactate transport in astroglial cells and monocarboxylate transporter 1 (MCT 1) expressing Xenopus laevis oocytes. Expression of two different monocarboxylate transporters in astroglial cells and neurons. *J Biol Chem*. 1997;272:30096-30102.
34. Ideno M, Kobayashi M, Sasaki S, *et al*. Involvement of monocarboxylate transporter 1 (SLC16A1) in the uptake of l-lactate in human astrocytes. *Life Sci*. 2018;192:110-114.
35. Woo J, Im SK, Chun H, *et al*. Functional characterization of resting and adenovirus-induced reactive astrocytes in three-dimensional culture. *Exp Neurobiol*. 2017;26:158-167.
36. Escartin C, Pierre K, Colin A, *et al*. Activation of astrocytes by CNTF induces metabolic plasticity and increases resistance to metabolic insults. *J Neurosci*. 2007;27:7094-7104.
37. Yun M, Bang SH, Kim JW, Park JY, Kim KS, Lee JD. The importance of acetyl coenzyme A synthetase for 11C-acetate uptake and cell survival in hepatocellular carcinoma. *J Nucl Med*. 2009;50:1222-1228.
38. Duong MT, Chen YJ, Doot RK, *et al*. Astrocyte activation imaging with 11C-acetate and amyloid PET in mild cognitive impairment due to Alzheimer pathology. *Nucl Med Commun*. 2021;42:1261-1269.
39. Leino RL, Gerhart DZ, van Bueren AM, McCall AL, Drewes LR. Ultrastructural localization of GLUT 1 and GLUT 3 glucose transporters in rat brain. *J Neurosci Res* 1997;49:617-626.
40. Zimmer ER, Parent MJ, Souza DG, *et al*. [(18)F]FDG PET signal is driven by astroglial glutamate transport. *Nat Neurosci*. 2017;20:393-395.
41. Xiang X, Wind K, Wiedemann T, *et al*. Microglial activation states drive glucose uptake and FDG-PET alterations in neurodegenerative diseases. *Sci Transl Med*. 2021;13:eabe5640.
42. Cheng J, Zhang R, Xu Z, *et al*. Early glycolytic reprogramming controls microglial inflammatory activation. *J Neuroinflammation*. 2021;18:129.
43. Ju YH, Bhalla M, Hyeon SJ, *et al*. Astrocytic urea cycle detoxifies aβ-derived ammonia while impairing memory in Alzheimer's disease. *Cell Metab*. 2022;34:1104-1120.e8.
44. Ko HY, Chung JI, Kim D, *et al*. Visualizing cancer-originated acetate uptake through MCT1 in reactive astrocytes demarcates tumor border and extends survival in glioblastoma patients. bioRxiv [Preprint] https://doi.org/10.1101/2021.04.13.439750.
45. Jin S, Cao Q, Yang F, *et al*. Brain ethanol metabolism by astrocytic ALDH2 drives the behavioural effects of ethanol intoxication. *Nat Metab*. 2021;3337-351.

46. Ferreira JM, Burnett AL, Rameau GA. Activity-dependent regulation of surface glucose transporter-3. *J Neurosci*. 2011;31: 1991-1999.
47. Patel AB, Lai JC, Chowdhury GM, *et al*. Direct evidence for activity-dependent glucose phosphorylation in neurons with implications for the astrocyte-to-neuron lactate shuttle. *Proc Natl Acad Sci U S A*. 2014;111:5385-5390.
48. Suzuki A, Stern SA, Bozdagi O, *et al*. Astrocyte-neuron lactate transport is required for long-term memory formation. *Cell*. 2011;144:810-823.
49. Wyss MT, Weber B, Treyer V, *et al*. Stimulation-induced increases of astrocytic oxidative metabolism in rats and humans investigated with 1-11C-acetate. *J Cereb Blood Flow Metab*. 2009; 29:44-56.
50. Yamamoto Y, Nishiyama Y, Kimura N, *et al*. 11C-acetate PET in the evaluation of brain glioma: Comparison with 11C-methionine and 18F-FDG-PET. *Mol Imaging Biol*. 2008;10: 281-287.
51. Kim S, Kim D, Kim SH, Park MA, Chang JH, Yun M. The roles of (11)C-acetate PET/CT in predicting tumor differentiation and survival in patients with cerebral glioma. *Eur J Nucl Med Mol Imaging*. 2018;45:1012-1020.
52. Saiki S, Sasazawa Y, Fujimaki M, *et al*. A metabolic profile of polyamines in Parkinson disease: A promising biomarker. *Ann Neurol*. 2019;86:251-263.
53. Sandusky-Beltran LA, Kovalenko A, Ma C, *et al*. Spermidine/spermine-N(1)-acetyltransferase ablation impacts tauopathy-induced polyamine stress response. *Alzheimers Res Ther*. 2019; 11:58.
54. Parthoens J, Servaes S, Verhaeghe J, Stroobants S, Staelens S. Prelimbic cortical injections of a GABA agonist and antagonist: In vivo quantification of the effect in the rat brain using [(18)F] FDG MicroPET. *Mol Imaging Biol*. 2015;17:856-864.
55. Colombo AV, Sadler RK, Llovera G, *et al*. Microbiota-derived short chain fatty acids modulate microglia and promote Aβ plaque deposition. *Elife*. 2021;10:e59826.
56. Erny D, Dokalis N, Mezo C, *et al*. Microbiota-derived acetate enables the metabolic fitness of the brain innate immune system during health and disease. *Cell Metab*. 2021;33:2260-2276.e7.
57. Liu J, Li H, Gong T, *et al*. Anti-neuroinflammatory effect of short-chain fatty acid acetate against Alzheimer's disease via upregulating GPR41 and inhibiting ERK/JNK/NF-kappaB. *J Agric Food Chem*. 2020;68:7152-7161.
58. Cagnin A, Brooks DJ, Kennedy AM, *et al*. In-vivo measurement of activated microglia in dementia. *Lancet*. 2001;358:461-467.
59. Surendranathan A, Su L, Mak E, *et al*. Early microglial activation and peripheral inflammation in dementia with Lewy bodies. *Brain*. 2018;141:3415-3427.
60. Passamonti L, Rodriguez PV, Hong YT, *et al*. [(11)C]PK11195 binding in Alzheimer disease and progressive supranuclear palsy. *Neurology*. 2018;90:e1989-e1996.
61. Gulyás B, Vas A, Toth M, *et al*. Age and disease related changes in the translocator protein (TSPO) system in the human brain: Positron emission tomography measurements with [11C]vinpocetine. *Neuroimage*. 2011;56:1111-1121.
62. Takano A, Piehl F, Hillert J, *et al*. In vivo TSPO imaging in patients with multiple sclerosis: A brain PET study with [18F]FEDAA1106. *EJNMMI Res*. 2013;3:30.
63. Golla SS, Boellaard R, Oikonen V, *et al*. Quantification of [18F] DPA-714 binding in the human brain: Initial studies in healthy controls and Alzheimer's disease patients. *J Cereb Blood Flow Metab*. 2015;35:766-772.
64. Varrone A, Mattsson P, Forsberg A, *et al*. In vivo imaging of the 18-kDa translocator protein (TSPO) with [18F]FEDAA1106 and PET does not show increased binding in Alzheimer's disease patients. *Eur J Nucl Med Mol Imaging*. 2013;40:921-931.
65. Villemagne VL, Harada R, Dore V, *et al*. Assessing reactive astrogliosis with (18)F-SMBT-1 across the Alzheimer's disease spectrum. *J Nucl Med*. 2022;63:1560-1569.
66. Harada R, Hayakawa Y, Ezura M, *et al*. (18)F-SMBT-1: A selective and reversible PET tracer for monoamine oxidase-B imaging. *J Nucl Med*. 2021;62:253-258.